Spring 2014

Raman Signal Enhancement for Low-Noise, Chemically Sensitive Imaging in Soft Matter Systems

Derek Gann
University of Colorado Boulder

Raman Signal Enhancement for Low-Noise, Chemically Sensitive Imaging in Soft Matter Systems

By

Derek Gann

Undergraduate Honors Thesis

Department of Physics

University of Colorado, Boulder

April 3rd, 2014

Thesis Advisor: Doctor Ivan Smalyukh (phys)

Field: Liquid Crystal Photonics and Imaging Studies

Degree: B.S. Engineering Physics

Expected Graduation: May, 2014

Committee Members: Doctors James Thompson (phys),

Thomas Schibli (phys), and Garret Moddel (ecee)

Table of contents

Abstract

We demonstrate the use of novel imaging techniques for studying a variety of soft condensed matter systems. The materials we use have applications in high-speed switchable devices, meta-materials, and photovoltaics to name a few. In all of these applications, the processes and structures in the underlying material are crucial for their operation. Because of this we are interested in developing methods for imaging liquid crystal-colloid systems that are highly sensitive to the position and orientation of various molecules and particles on the micron and sub-micron scale. We present unique imaging systems based on Raman-scattering confocal microscopy, which are useful in probing the spontaneous ordering of liquid crystals and colloidal nanoparticles in two unique ways. The first method employs a pump-probe technique to measure the loss in the pump beam due to stimulated emission by the probe on targeted molecular bonds, giving a significant ($\approx 10^6$) enhancement in signal. This provides a method for orientation sensitive, low noise, non-invasive imaging of our samples due to our ability to tune the probe beam frequency to the bond resonance while remaining below the fluorescence threshold. The second method makes use dispersed, gold “nano-burst” particles to amplify Raman signals via the principle of plasmonic resonance. We present a characterization of this resonant enhancement as well as how to manipulate these particles using holographic optical tweezers with rotational control. the effect varies due to different sample geometries, polarization dependencies, and molecular orientation.

1. Background and Current Imaging Techniques

1.1 Motivations

Liquid crystals (LCs) are complex states of soft-matter, with material properties between isotropic liquids and crystalline solids that were first scientifically investigated at the end of the 19th century. Since then, LCs have led to many new fields of study in biology, chemistry, physics, and electronics. Applications of LCs include the discovery and study of DNA structure and switchable optical devices, such as liquid crystal displays or spatial light modulators. LCs are also being explored for use in tunable lasers, which use the liquid crystal as a gain medium, engineerable and switchable nano-materials, and organic photo-voltaic devices, amongst others. In all of these applications the unique geometry and chemical composition of the LC devices play a large roll in the underlying and emergent physical properties of system. Because of this, others in the group wish to investigate fundamental physics of liquid crystals concerning the dispersion, manipulation, and self-assembly of various colloids, reactive materials, and crystalline defects. To aide in this effort we develop and demonstrate novel imaging techniques alongside the experimentation in order to probe these systems in novel and unique ways.

1.2 Liquid Crystal Media

Liquid crystals are a state of condensed matter that have properties between fully isotropic liquids and crystalline solids. They are free to flow like liquids, but maintain degrees of spatial and orientational ordering not seen in isotropic fluids. In terms of bulk properties, the positions and orientations of the atoms in an isotropic liquid are almost entirely uncorrelated with one another and as such the isotropic liquid retains the translational and rotational symmetries of free space. In other words, we can translate our view by any distance and rotate our view by any angle in the liquid and the material will look qualitatively the same everywhere, which can also be done with free/ empty space. For single-domain crystalline solids, the position and orientation of every atom is perfectly correlated with every other atom in a structure. We call this structure a crystalline lattice. In a lattice, there is a consistent orientation and even spacing between neighboring lattice sites (typically atomic positions, and also orientations if there is a dipole moment or molecular asymmetry). This is a form of spontaneous symmetry breaking since now the crystal geometry only retains a portion of the symmetries of free space, i.e. only translations and rotations by discrete values will return us to our original perspective [3]. See figure 1.2.1 for a visual representation of these properties. It is also generally assumed that atoms in a liquid are free to move about the material, while the atoms of a solid are thought of as being fixed at the lattice sites.

For many materials, such as water, upon cooling them as an isotropic fluid past some critical temperature there is a simple, first-order phase transition as the molecules freeze and lose degrees of freedom. If the molecules lock into a rigid array then a crystalline solid is produced [3]. In the late 1800's though, an Austrian botantist, Friedrich Reinitzer, found that cholesterol benzoate undergoes two phase transitions, one from a clear to a cloudy liquid

then finally from the cloudy liquid to a solid. Otto Lehman, a German physicist, then found that many lipids exhibit this intermediate liquid phase and determined that they maintain some degree of orientational ordering and anisotropy, properties of a solid. Lehman then coined the term liquid crystals, to succinctly describe the foreign states of matter. Since then, a variety of liquid crystalline species and phases have been discovered, as well as techniques for synthesizing LCs, to include room temperature LCs like 5CB [4]. They typically form out of disk or rod-shaped, intermediately sized organic molecules, whose Van-der-Waals interactions cause them to self-order in various ways due to their anisotropic geometry [4][7].

There are two overarching categories of liquid crystals, the thermotropic and lyotropic species. Thermotropic LCs are materials that undergo phase transitions only via changes in temperature. Typical thermotropic LC phases include the nematic, smectic, and cholesteric liquid crystalline phases. Lyotropic LCs are materials that do not only rely on temperature for ordering, but also on the concentration of the crystal forming solute in some dissolving medium. A micelle is a common example of a lyotropic LC phase [4][10]. In this paper I will focus on thermotropic liquid crystals as they are the species we use in the imaging studies I present here. However, the majority of the techniques and discussion are applicable to lyotropic species as well.

The orientational order in a LC is denoted by the vector $\hat{n}$, called the director, which typically lies along the long-range directional order of the molecules (see figure 1.2.1) [5][6]. This vector takes no preferred polarity, i.e. $\hat{n}=-\hat{n}$, since typically neither do the constituent molecules in the absence of an applied field [7]. For the nematic phase, the director is constant throughout the material thus giving an orientational ordering to the LC (figure 1.2.2 (a)). In the smectic LC phase, the director again lies in the same direction

everywhere but the molecules also align into layers, often with the director pointing at an angle to the normal of the layer planes (fig. 1.2.2 (b)). Another common phase is the so-called cholesteric phase (since cholesterols exhibit this phase), also known as the chiral nematic phase. In any one plane of the cholesteric LC the director structure looks like the nematic phase. However, as you translate in a direction perpendicular to the director, $\hat{n}$, begins to twist in a helical fashion. The direction of rotation determines the handedness of the cholesteric, and the distance it takes for the director to rotate by 360 degrees is called the pitch [5] [6] [3] [4] [10] [11] [12]. See figure 1.2.2 for an illustration of the phases mentioned above.

Just as with crystalline solids, there are circumstances that give rise to changes in the ordering in LC. One way to do this is to localize the LC to a surface that promotes alignment of the LC. This process is called surface anchoring. Anchoring occurs at most surfaces the LC encounters, but can also be controlled with specially prepared surfaces that force a particular alignment on the LC [7][12]. It has been shown that LC molecules will reorient in the presence of electric, magnetic, and optical fields too [6][10][13]. Additionally, liquid crystals often will relax into multiple domains when the director varies from one region to another. This can happen slowly in splays, twists, and bends of the director in what are called elastic distortions (see figure 1.2.3). Conversely, this can happen abruptly, resulting in a discontinuity of the director known as a defect. Depending on the type of distortion, these defects take on a value $\pm m/2$, a number which is related to the topology of the particular defect [7][9][10] [12]. If the LC director rotates by 2π as you go a full revolution around the defect then the defect gets a ± 1 . If the LC director only rotates by π , then the defect is $\pm\frac{1}{2}$. See

figure 1.2.4 for an illustration of common defects that occur in nematic LCs.

The director structure is then often the topic of interest in studying liquid crystals, as the geometry determines the physical properties of the material. As such, various techniques are employed to image this structure within the bulk of a LC.

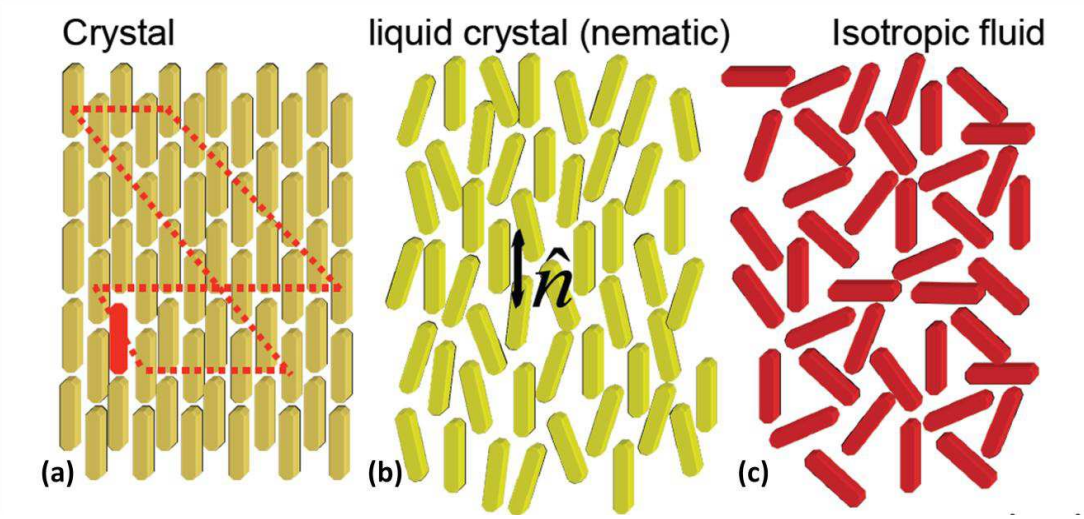

Figure 1.2.1. Above is a cartoon depicting the differences between (a) solid, (b) nematic liquid crystal, and (c) isotropic liquid phases of matter. The dashed lines in (a) represent translational symmetries of the solid and the molecules are drawn as rods to represent orientational ordering. The vector drawn in (b) shows the director $\hat{n}$ which lies along the long range orientational order of the nematic LC. In (c) we see that there is no special ordering of the isotropic fluid.

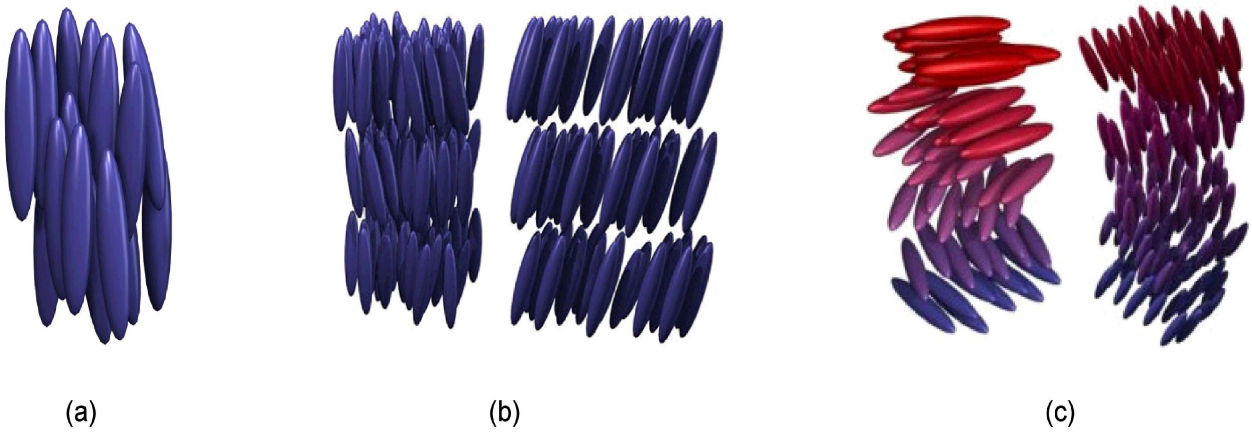

Figure 1.2.2. Above is an illustration of molecular ordering for (a) the nematic, (b) the smetic a and c, and (c) the chiral nematic liquid crystal phases. Image adapted from The Analysis of Liquid Crystal Phases using Polarized Optical Microscopy" by C. Xiang, (2011).

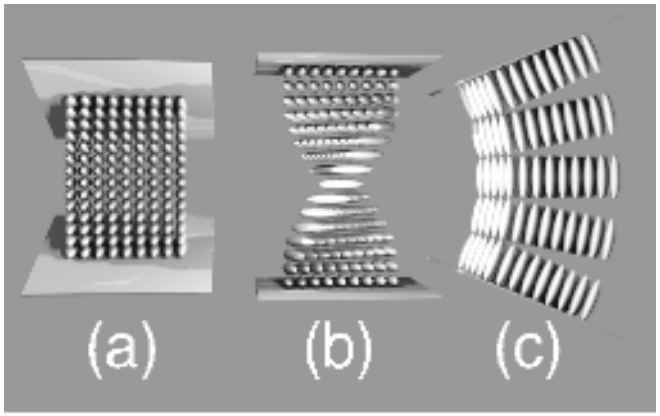

Figure 1.2.3. Cartoon representation of elastic distortions occurring in a nematic LC in the form of splaying (a), twisting (b), and bending (c). Adapted from "Overview of the mesoscopic theory of liquid crystals," by Harald Ehrentraut, *Institut für Theoretische Physik* (1997)

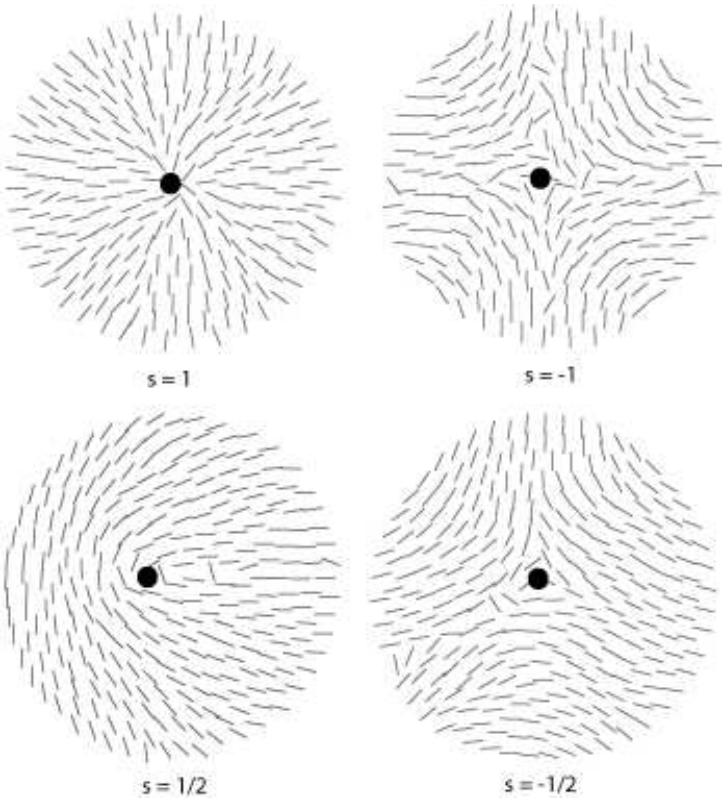

Figure 1.2.4. Drawings showing director discontinuity around ± 1 and $\pm 1/2$ defects in a nematic LC. Adapted from "Defects," *Liquid Crystals*, a DoITPoMS sponsored by the University of Cambridge, and licensed under Creative Commons, (2008), accessed on March 19, 2014

1.3 Polarizing microscopy

Polarizing microscopy (PM) is the use of optical microscopes with polarizing elements to probe how light interacts with a material of interest. For example, due to the anisotropy of liquid crystal molecules, light will interact with the material differently depending on how it is polarized. Anisotropy implies that there is a broken symmetry in the material; in this case it is the uneven shape of rod and disk-like molecules. For uniaxial crystals, we call the axis along which symmetry is broken the optical axis of the material, see figure 1.3.1. Our liquid crystal director, $\hat{n}$, is then the average of the molecular optical axes. We call materials with this uni-axially broken symmetry birefringent because they often will exhibit two distinct indices of refraction for incident light. Specifically, light polarized along the optical axis will respond differently than light polarized along either of the other two axes which are orthogonal to the optical axis and look similar to each other. Via the wave nature of light, any arbitrary polarization can then be decomposed into components along these various axes of the birefringent material.

A common PM technique is to use two so-called crossed polarizers, where one is used to polarize a light source that then interacts with the material of interest and comes out with an unknown polarization. The second polarizer, often referred to as the analyzer, then probes the outgoing light in order to gain information about the structure of a birefringent material. Figure 1.3.2 illustrates the concept of the polarizer-analyzer technique.

If we use this technique on a nematic LC with the polarizer and analyzer at 90 degrees to one another and the bulk LC director (also known as the “far-field” director) at 45 degrees to the polarizers, we can obtain images like figure 1.3.3. If the liquid crystal director lies along the polarizer axis or at 90 degrees to it (along the analyzer), then incident light will only see

one index of refraction and the light will exit the crystal with its polarization unchanged. As a consequence, the analyzer, which is sitting orthogonal to the original polarization, will block all of the outgoing light for these director orientations and the image will appear dark in these places (Malus' law). For director orientations between the polarizer and analyzer angles, the incident light sees both of the refractive indices. This induces a phase shift and change in relative amplitude between the component along the optical axis and its orthogonal compliment. Upon exiting the material, this light now has a different polarization from the incident beam and as such does not get blocked by the analyzer. With this in mind, we can understand the convergent points in figure 1.3.3 as the ± 1 and $\pm 1/2$ defects shown in figure 1.2.4, with four and two dark brushes due to director rotation of 2π and π, respectively.

To get more sophisticated information of the director with additional analysis, this technique can be improved upon by the addition of a wave-plate before the analyzer or after the polarizer. However, despite its usefulness in being able to image the director structure, interaction of the focused light occurs throughout the whole sample (see figure 1.4.1) and because of this, the use of PM alone is limited to two-dimensional imaging of thin soft matter samples. Due to this limitation, a number of improvements on the PM technique have been developed.

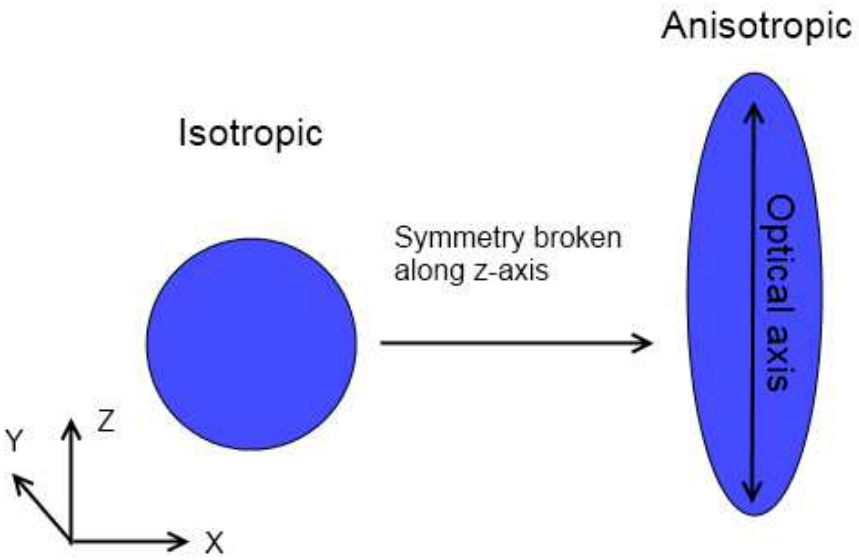

Figure 1.3.1 A cartoon demonstrating the concept of symmetry breaking in anisotropic materials, leading to the distinction of a unique optical axis and birefringent response of materials.

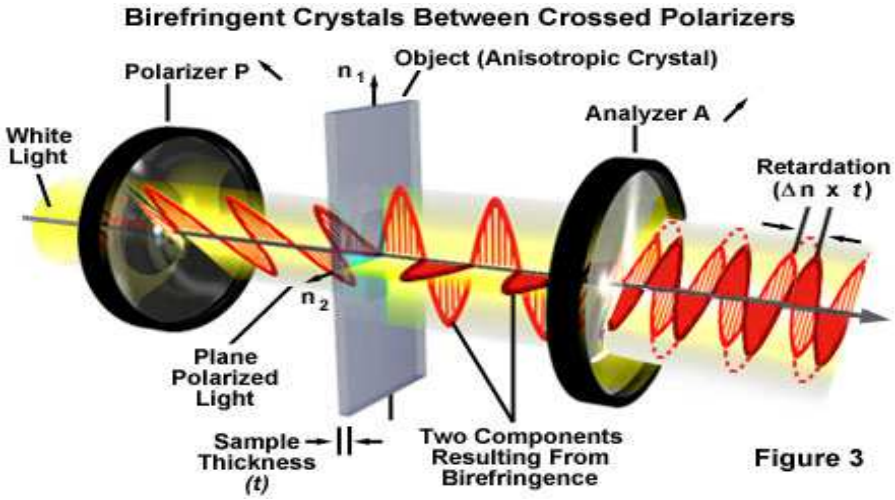

Figure 1.3.2. This illustration demonstrates the concept of polarizing optical microscopy and its use in studying birefringent materials. Adapted from "Introduction to Optical Birefringence" by Murphy et. al. on Nikon's MicroscopyU™ (2013), <http://www.microscopyu.com/articles/polarized/birefringenceintro.html>, accessed on March 22, 2014.

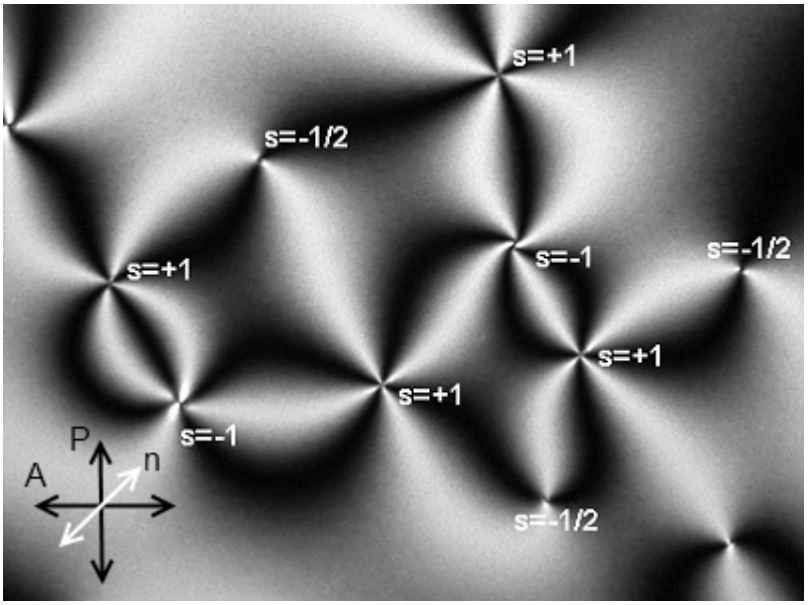

Figure 1.3.3. This image shows actual polarized microscopy images of nematic LC in between crossed polarizers. In the image we see the “brush” patterns characteristic of +/-1 and +/-1/2 defects which form in the nematic bulk. This is the so-called “Schlieren texture.” Adapted from “8. Textures of Liquid Crystals” in *Liquid Crystals: a Simple View on a Complex Matter* by Bohdan Senyuk, Kent State University (2006).

1.4 Confocal Polarizing Microscopy

This technique has many advantages over conventional polarizing microscopy that stem from its ability to obtain images at a single focal plane, thus increasing resolution and minimizing additional signal from out-of-focus depths of the sample. One method realizes this by focusing an illumination source onto a sample and collecting the emitted light by the same, or a secondary, objective. The collecting objective focuses the diverging light of the sample at different positions for various parts of the sample. Light emitted by the sample from the focal point of the collecting lens gets collimated, while out of focus planes remain divergent. A second pinhole can then be placed at the focal point of another lens which only the collimated beam will be properly focused on, thereby spatially separating the in focus plane and out of focus planes. When this happens, we say the filtering pinhole is confocal to the image plane of the sample. Figure 1.4.1 shows a schematic of a basic confocal setup. Other optical elements, like dichroic mirrors and filters or polarization retarders, are then usually placed between the collecting objective and the detector to separate the excitation light from the signal of interest.

Since confocal microscopy allows experimenters to collect light from single planes of a sample, it can be used to construct three-dimensional images of the LC director structure by scanning through a series of planes. However, due to the fact that you are now excluding a large portion of the signal, i.e. since only a small portion of your excitation light interacts with the focal plane, confocal PM typically requires the use of invasive dyes that give strong fluorescence to be introduced to the system. In order to even be effective, the dye molecules have to be anisotropic so that they lie along the LC director, have a fluorescence transition along this anisotropic axis to allow for polarized imaging of the director, and they must have

easily separable excitation and emission spectra. These difficulties, along with the possible distortion of your sample geometry, make the use of dyes unfavorable when trying to image delicate, soft-matter systems.

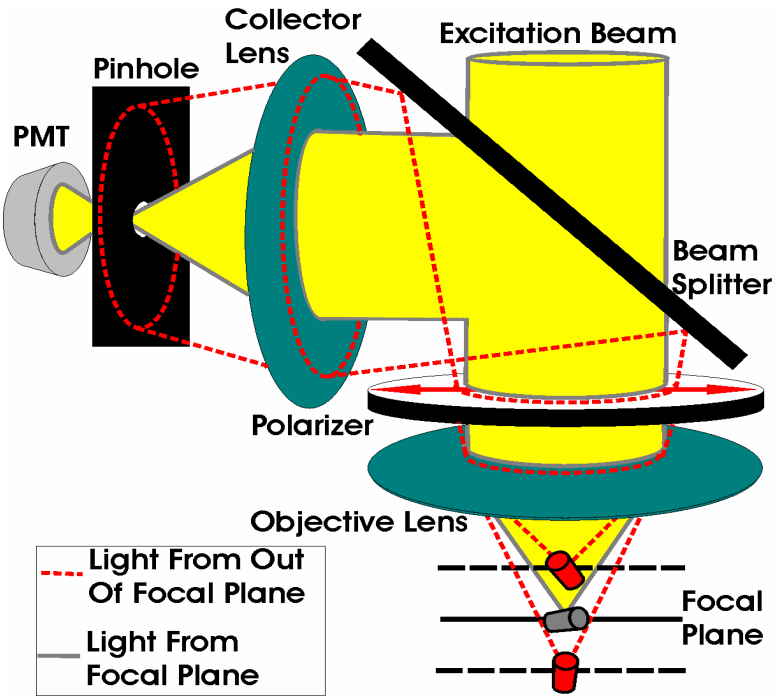

Figure 1.4.1 Schematic of the geometric principles behind confocal microscopy. Adapted from "Focused laser beams and liquid crystals: fast three-dimensional imaging of structures and topological defects" by I. Smalyukh et. al. (2005).

1.5 Multiple Photon Fluorescence

We can avoid the issues of low confocal signal and having to introduce invasive dyes by moving to higher order optical processes, i.e. the use of multiple excitation photons to produce a single signal photon. One such process is multiple photon fluorescence (MPF), which is when two photons of half the energy excite the same transition of a single photon; see figure 1.5.1. This can be extended to n photons each with 1/n as much energy as it takes to excite fluorescence. This allows for intrinsic separation of excitation and emission light. Also, due to it being a non-linear optical process the signal intensity is proportional to excitation power to the number of photons involved n, i.e.

$$I_{signal} \propto P^{n}_{excitation}$$ [15].

The probability of multiple absorption events is typically quite small, which is both good and bad. This combined with the non-linear signal response means that fluorescence will only be significantly excited at the focus of the excitation beam where the laser intensities are very high. This provides intrinsic, three-dimensional resolution to the imaging system; see figure 1.5.2. However, this also requires the use of expensive, pulsed laser sources to achieve the necessary instantaneous powers needed to acquire sufficient signal from the sample. There are also concerns of heating the sample due to the resonant energy transfer between molecules (depicted as the fine-line transitions in the excited state in figure 1.5.1), which can potentially cause distortion of the sample you wish to image.

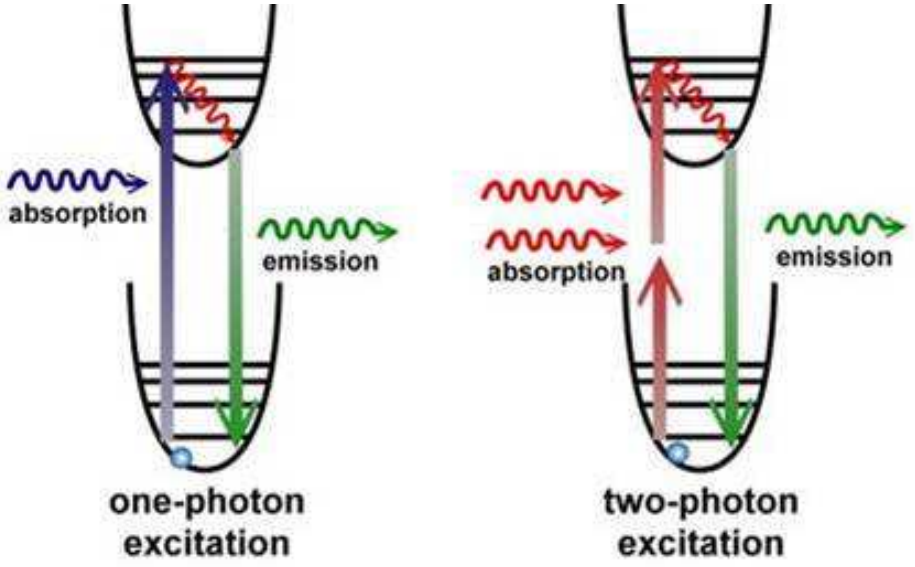

Figure 1.5.1. A cartoon depicting energy transitions in a single (left) and two-photon (right) excitation event. The two excitation photons on the right have exactly half the energy as the single excitation photon on the left. This is an example of second-harmonic generation in a fluorescing molecule, a type of non-linear optical process.

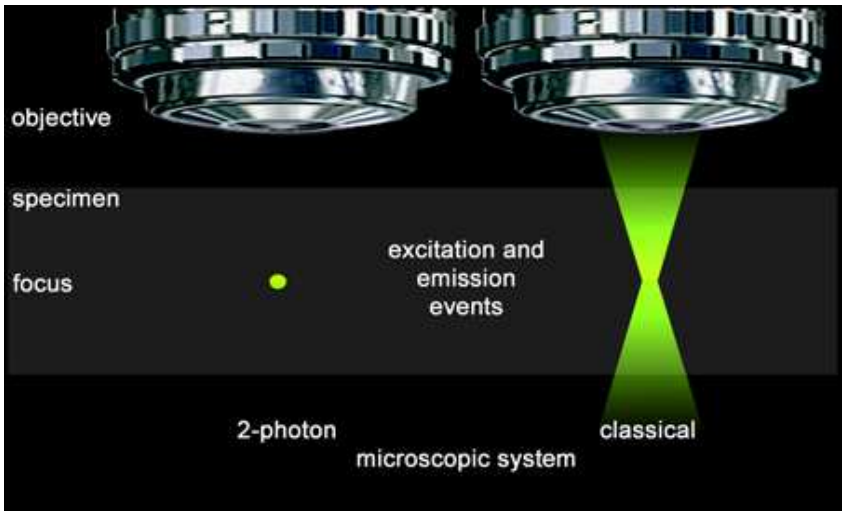

Figure 1.5.2. An illustration comparing the excitation/ emission profiles between conventional wide-field, fluorescence microscopy and two-photon fluorescence. The disparity arises due to the non-linear nature and necessity of multiple absorptions in the two-photon process.

1.6 Raman Scattering

Raman scattering, first discovered by C. V. Raman in 1928, is the inelastic scattering of light off of matter [16]. During this process the light can either lose or gain energy due to resonant interaction with molecules in the medium, as opposed to scattering with the same energy. The interaction can be thought of simply as the interaction between the oscillating electric field component of incident light and a bond vibration with variable polarizability (such as the symmetric vibrational mode of CO2) [19]. The polarizability tells us the degree to which a molecule gets distorted in an electric field, and thus the bond polarizability determines the relative susceptibility to Raman scattering. This is the selection rule for a mode to be Raman active, i.e. that the has to have a variable polarizability in order to interact with the oscillating electric field of incident light [19][22]. The oscillating field then can drive this vibration, which we often visualize as the stretching and bending between the atoms comprising the bond [16] [19][22]. Since these vibrations occur along specific molecular axes, Raman scattering combined with PM can also be exploited if you know the geometry and Raman spectrum of your material of interest [17] [18] [19].

It turns out that these bonds act like quantized harmonic oscillators and thus accept and emit photons only at discrete energies. When an incident photon puts energy into the oscillator and then scatters we have a Stokes-Raman event, as shown in figure 1.6.1. With the energy of the molecular vibrational quanta given by $\hbar\omega_{vibrational}$ and the energy of the incident photon given by $\hbar\omega_{incident}$, we then have that the emitted, Stokes-shifted photon has energy.

$$\hbar\omega_{emitted} = \hbar\omega_{incident} - \hbar\omega_{vibrational} .$$

When the reverse process occurs, i.e. an excited bond adds energy to an incident photon, we have an anti-Stokes scattering event with energy,

$$\hbar\omega_{emitted} = \hbar\omega_{incident} + \hbar\omega_{vibrational} \quad .$$

If there is no interaction with the vibrational mode we have a Rayleigh scattering event, where

$$\hbar\omega_{emitted} = \hbar\omega_{incident} \quad .$$

Due to the energy shift of the Raman scattered photons, dichroic filters can be used to separate the incident and emitted light by choosing an edge pass with a cutoff frequency between $\hbar\omega_{emitted}$ and $\hbar\omega_{incident}$ to see Raman scattered light. With appropriate optics, the scattered light can then be used to gain positional information of the chemical producing the shifts.

The discrete transitions produce sharp peaks which happen to be quite unique amongst various molecules as well as the various bonds within molecules. A Raman spectrum and molecular geometry for the 5CB LC is shown in figure 1.6.2. Also labeled in the figure are the characteristic stretching vibrations of the CC bond between the benzene rings and the CN bond. Both of these vibrations lie along the molecular axis and as such can be used to determine the LC director. This could potentially allow for chemically specific imaging if the system could be tuned to sense only specific Raman energy shifts.

These shifts, however, rely on transitioning through a “virtual state” (figure 1.6.1), termed “virtual” because it is not an eigenstate (allowed state) of the interacting system. Since they are undesirable states for the system to be in, the virtual states are infrequent and short lived, which in turn gives a relatively low probability for a Raman scattering event to occur. Typical scattering frequencies are one Stokes-Raman scattered photon per 10^10 scattering

events. Thus using conventional Raman scattering microscopy is insufficient to construct images of samples because the acquisition times would have to be enormous.

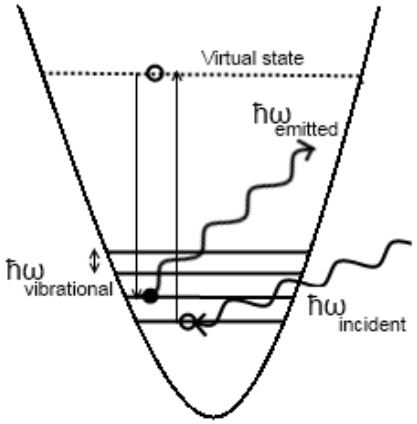

Figure 1.6.1 A cartoon demonstrating energy transitions in a Stokes-Raman scattering event. An incident photon electronically excites a polarized molecular bond into a disallowed or so-called "virtual" energy state. If the bond then relaxes to a higher, quantized vibrational state, a Stokes-Raman event occurs.

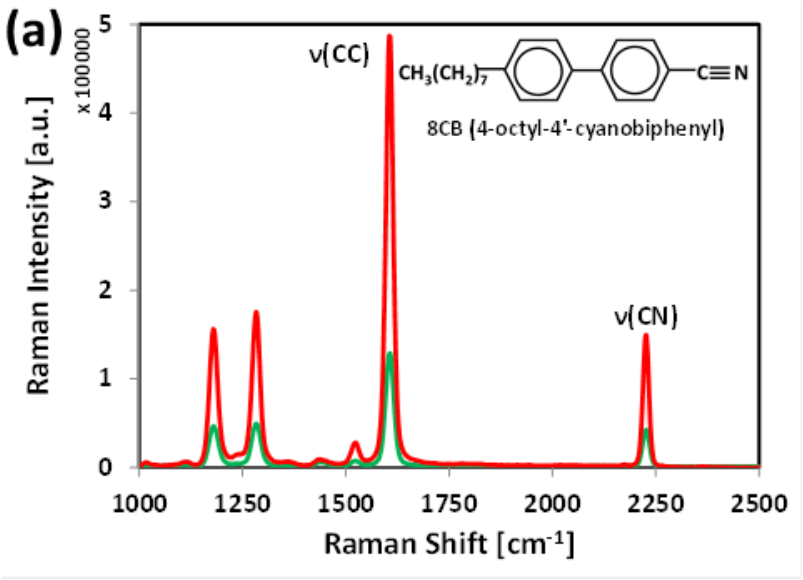

Figure 1.6.2. A plot of 8CB liquid crystal's Raman spectra in signal intensity (in arbitrary units) vs. the Raman shift wavenumber (in inverse cm). The large peak in the center corresponds to the characteristic stretching vibration of the CC bond between the benzene rings, and the peak on the right corresponds to the CN stretching vibration. The spectra were taken in nematic LC for excitation polarizations along (red) and perpendicular to (green) the far field director. Adapted from "Imaging of director fields in liquid crystals using stimulated Raman scattering microscopy," by T. Lee, H. Mundoor, D. Gann, T. Callahan, and I. Smalyukh (2013).

1.7 Stimulated Emission and Pump-Probe Technique

Various signal enhancement techniques are employed in order to combat the weak Raman signal. One common method relies on the process of stimulated emission that is driven by a pump-probe laser apparatus. Stimulated emission is the process whereby propagating light resonates with an excited electronic state and transitions it to the ground state, e.g. it has the same energy as the electronic transition, which causes the electron to relax and emit an additional photon of the same energy. For a pump-probe experiment, there are active components causing these excitations and stimulated emissions, the pump and the probe.

First, the pumping laser beam is focused onto a sample in order to raise the electron population from a lower (usually ground) state into an excited state. A probing laser is then sent in to the sample with a frequency tuned to the desired emission. In the context of enhancing a Raman scattering event, we could choose any $\hbar\omega_{pump}$ and $\hbar\omega_{probe}$ so that neither will excite fluorescing states and so that they will also have a difference equal to $\hbar\omega_{vibrational}$. This allows us to use the pump beam to push the bond of interest into the virtual state and then the probe beam stimulates the transition into the excited vibrational state. For example, if this were to be done with the oscillator in figure 1.6.1, the pump beam would have energy $\hbar\omega_{incident}$ and the probe beam would have energy $\hbar\omega_{emitted}$.

Typical enhancements from this technique are often on the order of 10^6, giving us a Raman scattering event on the order of 1 in 10^4 instead of 1 in 10^{10} incident photons. This increased signal, provided by stimulated emission, typically produces a sufficient number of Raman-shifted photons for the construction of an image of the LC director structure. Due to this being a second order, i.e. two photon, process like two-photon fluorescence, the signal

intensity is proportional to the product of powers, $P_{pump} * P_{probe}$. This again provides for intrinsic three-dimensional resolution without the use of a confocal pinhole and objective, since interaction only happens at the high intensity focus.

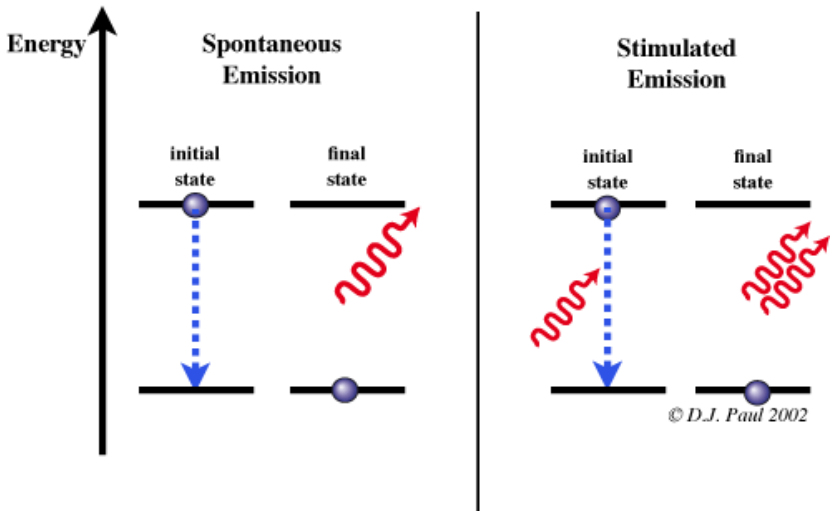

Figure 1.5.1. Schematic of the concept behind stimulated emission, whereby an incident photon promotes the relaxation of an electron to produce a second identical photon, i.e. with the same frequency and phase. Adapted from "Stimulated emission," *Si/SiGe Quantum Cascade Lasers*, by D. J. Paul, accessed at <http://userweb.eng.gla.ac.uk/d/dpaul/QCL/stimulated.html> on March 19, 2014

1.8 Coherent Anti-Stokes Raman Scattering

Coherent Anti-Stokes Raman Scattering (CARS) is one such pump-probe technique based on anti-Stokes Raman transitions that uses three photons. One photon, the pumping beam, is used to excite the bond to a virtual state. A second, the so-called Stokes beam, is then used to promote the transition of the bond into an excited state, i.e. $E_{pump} - E_{stokes} = E_{vibrational}$. A probe photon, often from the same beam as the pump, then anti-Stokes scatters off of the excited bond to produce an up-shifted photon above the probing frequency. See figure 1.8.1 (a) for a schematic of these transitions. This anti-Stokes shifted signal is then collected to form an image [17] [18] [20] [1]. Since this is a three photon event, the signal intensity is proportional to $P_{pump} * P_{stokes} * P_{probe}$, and provides a significantly enhanced signal.

On the other hand, the anti-Stokes Raman peaks are not as sharp as their Stokes shifted counterparts. Also the system often must be implemented in broad bands, i.e. spectrally broad excitation and collection, in order to acquire adequate signal from promoting transitions into multiple vibrational energy levels; see figure 1.8.1(b). This prevents us from doing really chemically specific imaging, as the CARS signals from multiple chemical species may be overlapping spectrally. There is also significant noise from other non-resonant processes due to the signal collection over broad bands.

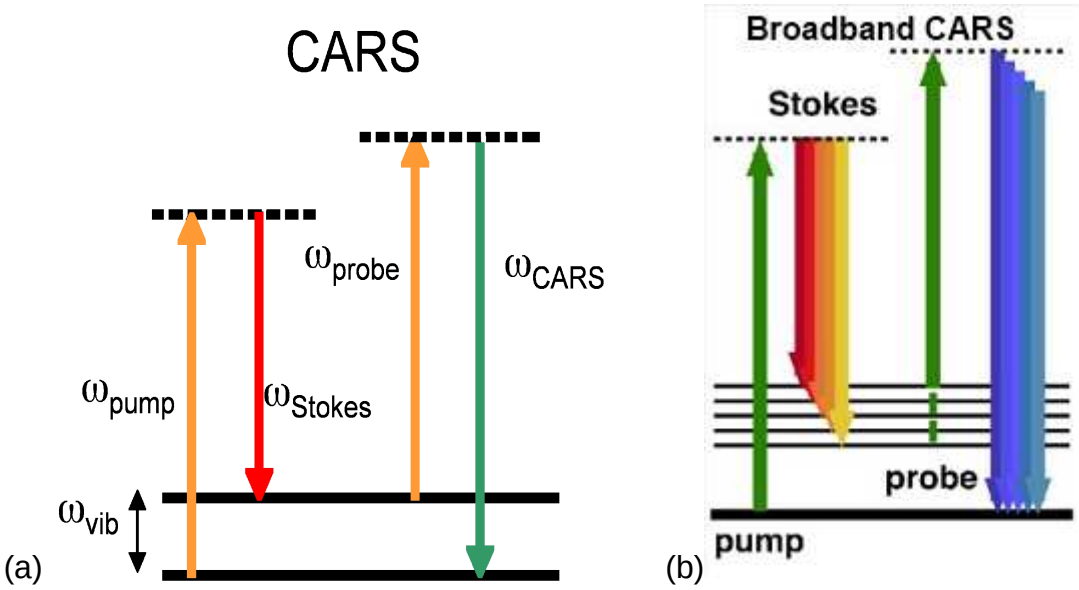

Figure 1.8.1. An illustration (a) of the three photon transitions required to produce the single anti-stokes shifted signal photon ω_{CARS}, e.g. a pumping transition, a stimulated emission to achieve molecular vibration, and a probing transition to give the shifted photon. Adapted from "Coherent Anti-Stokes Raman Scattering," en.Wikipedia.org, accessed from http://en.wikipedia.org/wiki/Coherent_anti-Stokes_Raman_spectroscopy on March 25, 2014.

(b) An illustration showing a broadband implementation of the same CARS, pump-probe technique. In this technique a broad Stokes beam is used to promote transitions to multiple different excited vibrational states to give a larger population for anit-Stokes Raman scattering. Adapted from "Coherent anti-Stokes Raman scattering (CARS) spectro-microscopy," by Dr. Misca Bonn, accessed from **http://www2.mpip-mainz.mpg.de/groups/bonn/research/bonn_mischa/cars_spectroscopy** on March 26, 2014.

2. Imaging Based on Stimulated Raman Loss

2.1 Idea and Motivation

We would like to be able to image the LC director, as well as the presence and orientations of other chemical species, without the use of invasive species while also limiting potential heating the LC and non-resonant background noise. Confocal microscopy with fluorescing dyes is out of the question due to the possibility of the dye molecules distorting the sample geometry. Multiple photon fluorescence isn't capable of sensitively distinguishing between chemical species with overlapping fluorescence emission spectra, and can lead to non-negligible heating of the sample and thus director distortion. Broadband CARS, although it can image in three dimensions with minimal heating, relies on relatively broad anti-Stokes Raman peaks, excitation by broad bands, and collection over a wide range of wavelengths, which make it fairly noisy due from non-linear background and also lacking in chemical sensitivity. To avoid these limitations we decided to implement imaging based on the Stokes Raman transitions. In order to obtain sufficient signal, we again used a pump-probe technique, but only with the pumping and Stokes transition beams so that signal intensity, I_{signal}, is proportional to $N*\sigma_{Raman}*P_{pump}*P_{stokes}$ and not $N*\sigma_{raman}*P_{pump}*P_{stokes}*P_{probe}$.

In order to leave the chemical sensitivity of this technique intact we do not implement the system in broadband. But because of this and the lower order of the optical process, the stimulated Raman signal is still too weak for direct acquisition. So for constructing images of the LC director, a thoughtfully designed experimental apparatus had to be developed.

2.2 Implementation of Stimulated Raman Loss Imaging

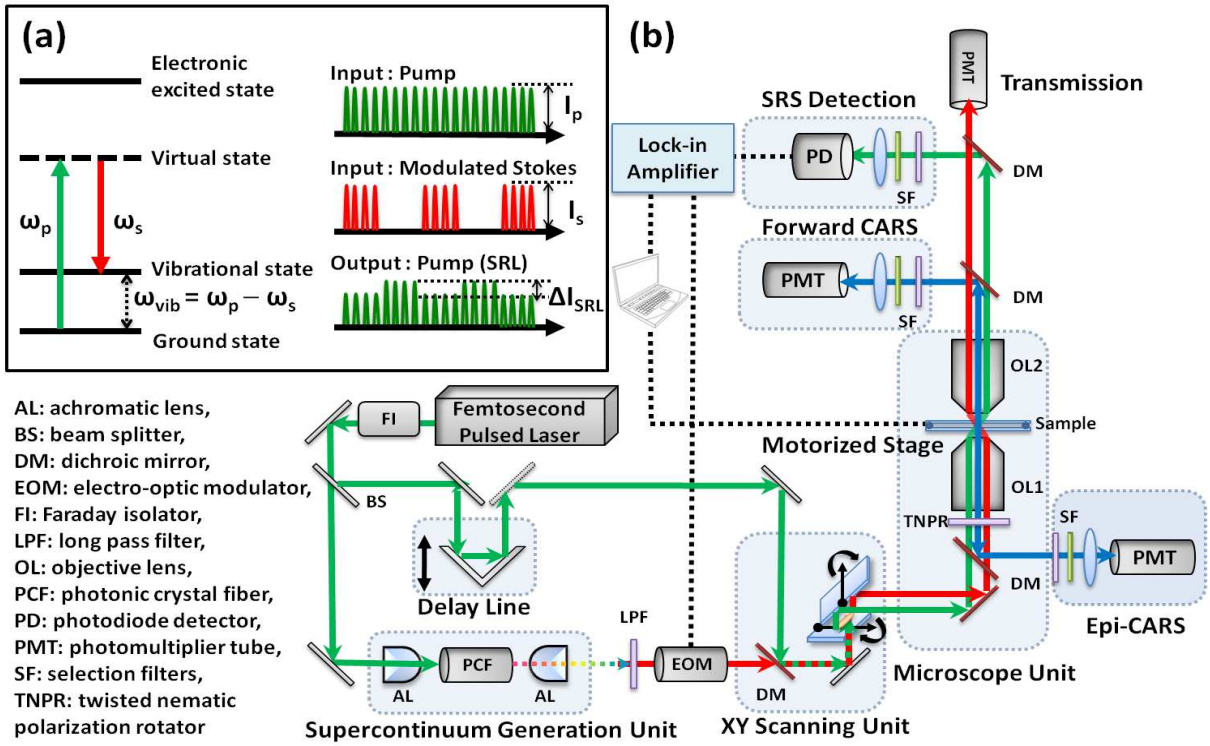

Figure 2.2.1 An illustration detailing the major components of the stimulated Raman loss (SRL) microscope. The concept is to use a single pulsed laser with a photonic fiber to produce a fixed pump and arbitrary Stokes frequency which can then be scanned over the sample to produce a stimulated Stokes emission. The Stokes beam is modulated for lock-in amplification, and loss in the pump scattering is detected upon stimulated emission. Adapted from “Imaging of director fields in liquid crystals using stimulated Raman scattering microscopy,” by T. Lee, H. Mundoor, D. Gann, T. Callahan, and I. Smalyukh (2013).

The setup we developed for imaging based on stimulated Raman scattering was designed as follows; refer to figure 2.2.1 for an illustration of the imaging apparatus. We use a femtosecond pulsed laser, to achieve the necessary instantaneous powers for significant Raman excitation, which is first split into two beam paths. One of the beams is used to excite a polarization maintaining, photonic crystal fiber to give a so-called super continuum, i.e. a very spectrally broad outgoing beam. The super continuum is then filtered to give a beam of the desired wavelength. This is the Stokes beam that produces our stimulated emission. The other beam that maintains the laser wavelength is the pump, which is recombined with the

Stokes beam after being sent through a delay line to phase-match their pulses. The beams go through fast scanning optics and are directed to the sample to produce the stimulated emission.

Conveniently, since this is the first step in CARS microscopy, additional scattering of pump photons off of the now excited, molecular vibrations allows us to detect a CARS signal as well. The scattered light is then collected and filtered into anti-Stokes, Stokes, and Rayleigh scattered beams. The anti-Stokes signal is collected in forward and reverse (“epi”) directions for more efficient collection. In order to improve our measurement sensitivity of the pump beam, we modulate the Stokes beam with an electro-optical modulator. When the Stokes beam turns on it will stimulate significant emission at the Stokes frequency as the molecular oscillators relax into an excited vibrational state, instead of simply Rayleigh scattering the pump photons. Coincidentally there will be roughly as many less photons proportionally in the scattered pump light. We then detect the pump signal via a lock-in amplifier which is frequency and phase matched to the modulated signal. This allows us to sensitively measure the pump loss, ΔI_{SRL}, that occurs when the Stokes beam turns on. Since we are measuring loss in the pump beam due to a stimulated Raman event, we term this technique stimulated Raman loss (SRL) microscopy.

However, even with stimulated emission and lock-in amplification, the pump signal loss ΔI_{SRL} is still too weak for fast imaging of the LC director. As such, custom software is used to run a step-wise slow scan with the motorized stage which also triggers the data acquisition from the amplifier. This allows us to control the relatively long pixel dwell times and lock-in integration times during the scanning of the sample, and also to synchronize this with data acquisition so that we can later reconstruct an image from the acquired SRL signal. [1]

2.3 Characterization of the SRL microscope

We ran several tests to characterize the system's response to variations of certain tunable parameters. We first took Raman spectra of our material of interest, the 8CB liquid crystal. The sample we prepared for this was a thin (15-30 μm) cell with planar boundary conditions, so that the LC would more or less uniformly sit along one direction. The spectra are given in figure 2.3.1(a) and the inset shows a simplified schematic of the 8CB molecule. The spectra show the un-stimulated Raman energy shifts off of the laser frequency in inverse centimeters, and the relative intensities for pump polarizations along the LC director (red) and perpendicular to the far-field director (green). We see there is about a three times larger signal for light polarized along the long molecular axis.

Then since we are using a second order/ two-photon process with two independent beams, we expect that signal intensity

$$\Delta I_{SRL} \propto N * \sigma_{raman} * P_{pump} * P_{stokes} \quad .$$

So for a fixed Stokes beam power and beam profile we expect that signal intensity

$$\Delta I_{SRL} \propto const * P_{pump} \quad ,$$

i.e. a linear dependence of SRL signal on pump power. From this we also expect that signal intensity

$$\Delta I_{SRL} \propto const\, P_{pump} * P_{stokes} \quad ,$$

i.e. a linear dependence on the product of pump and Stokes powers. This is precisely the dependence we see and figure 2.3.1 (b) and (c) show these two linear dependencies for 5 different powers or products of powers, respectively. These plots tell us we are indeed witnessing a second order optical process.

Finally, we show the dependence of the SRL signal on the angle between the excitation beams (both at the same polarization) and the far-field LC director. We see that as their relative angle goes from 0 degrees to 90, the SRL signal nearly vanishes. This shows that this method can be used to reliably determine director orientation. [1]

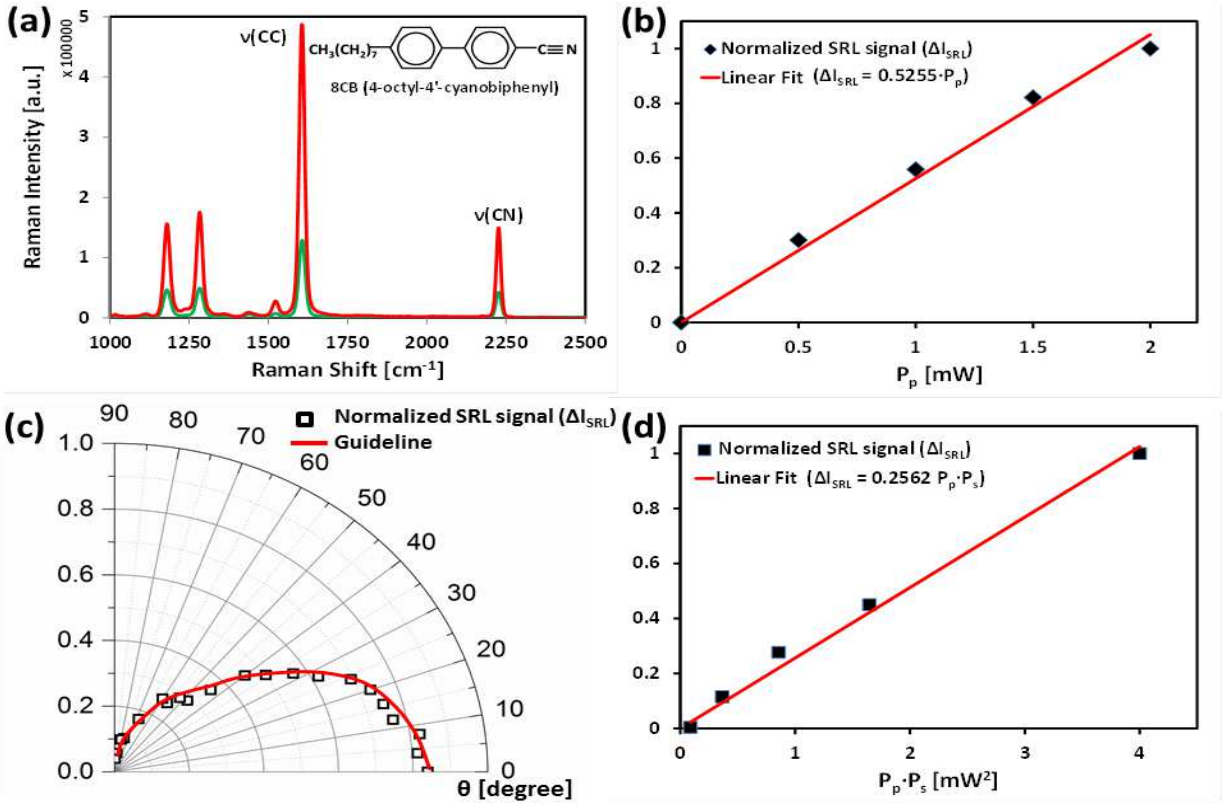

Figure 2.3.1 These are plots showing characteristics of the SRL microscope. Figure (a) show the Raman shifts for the 8CB LC molecule for two orthogonal polarizations, along (red) and perpendicular to (green) the far field director. Two of the peaks are labeled with their corresponding bond. The inset in (a) shows a simple drawing of the molecular geometry of 8CB. Figure (b) shows the linear dependence of ΔI_{SRL}, the signal power, on the pump power when the Stokes power is held fixed. Figure (d) shows the linear dependence of the SRL signal on the product of pump and Stokes powers. Figure (c) shows the extinction of SRL signal as the excitation polarizations go from aligned with the LC director to being orthogonal to it. Adapted from "Imaging of director fields in liquid crystals using stimulated Raman scattering microscopy," by T. Lee, H. Mundoor, D. Gann, T. Callahan, and I. Smalyukh (2013).

2.4 SRL Imaging Results

To demonstrate the applicability of this type of imaging, we present images of two well known LC geometries. Again using the 8CB LC, which is a smectic LC at room temperature, we first put it into a thin cell with homeotropic boundary conditions, i.e. chemically treated substrates that force the LC to align normal to the surface. In these conditions, it is typical to have a paired defect structure form known as a focal conic domain (FCD) [14]. One realization of the FCD has an elliptical defect line wrapped around a hyperbolic line defect. This is depicted in figure 2.4.1 (e) and (f). In (e) the lines lie along the average LC director and in (f) the sheets show the smectic layers which lie perpendicular to the director.

What we imaged is a cross section of the FCD in the plane of the ellipse. Figures 2.4.1 (a) and (b) show SRL images for two orthogonal polarizations collected using our microscope setup as detailed above. The bright areas in the images show regions where the LC director lies along the polarization axis. Figure 2.4.1 (c) is a superposition of (a) and (b) and effectively shows us the radial director structure in the center of the FCD, just as we expect. Figure 2.4.1 (d) shows a complementary image taken with CARS microscopy of the same FCD.

Another typical geometry encountered in LC systems are distortions and defects that are induced by colloidal particles. To demonstrate imaging of such a system, we prepared another thin sample with 8CB LC but this time imposed planar boundary conditions to produce a consistent far-field director, indicated by the rub direction in figure 2.4.2 (b). Additionally we included micrometer-sized, melanin resin beads, also with planar boundary conditions in order to induce a distortion in the director structure. The planar surface anchoring to the colloidal sphere is most incompatible with the LC director on the ends of the sphere, where the bulk LC wants to sit left-right but the surface requires the molecules to lie

up-down. This causes the production of two point defects on opposite sides of the resin sphere, two line defects extending from these points, and the surrounding distortions of the director structure. An illustration of this defect production and director distortion is given in figure 2.4.2 (b). The lines show the smectic layering of the 8CB LC, to which the LC director is perpendicular. Figure 2.4.2 (a) shows an SRL image we took of this type of colloidal distortion, demonstrating that SRL microscopy is capable of imaging LC-colloidal interactions as well. [1]

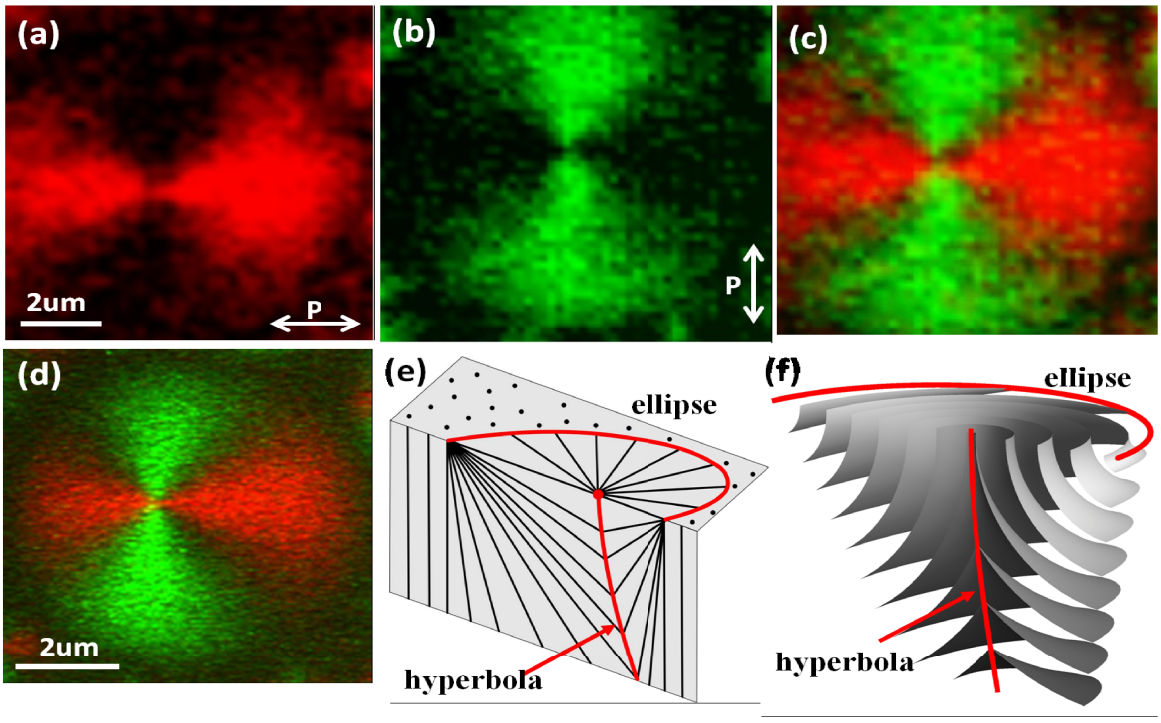

Figure 2.4.1 (a) and (b) show SRL microscopy images taken of a focal conic domain, in an elliptical cross-section, for two orthogonal polarizations. (c) shows their superposition and the radial director structure of the elliptical cross-section. (d) is a CARS microscopy image showing complementary information of the same focal conic domain. (e) and (f) depict the director structure and the smectic layering, respectively, for a focal conic domain consisting of an elliptical line defect encircling a hyperbolic line defect. Adapted from “Imaging of director fields in liquid crystals using stimulated Raman scattering microscopy,” by T. Lee, H. Mundoor, D. Gann, T. Callahan, and I. Smalyukh (2013).

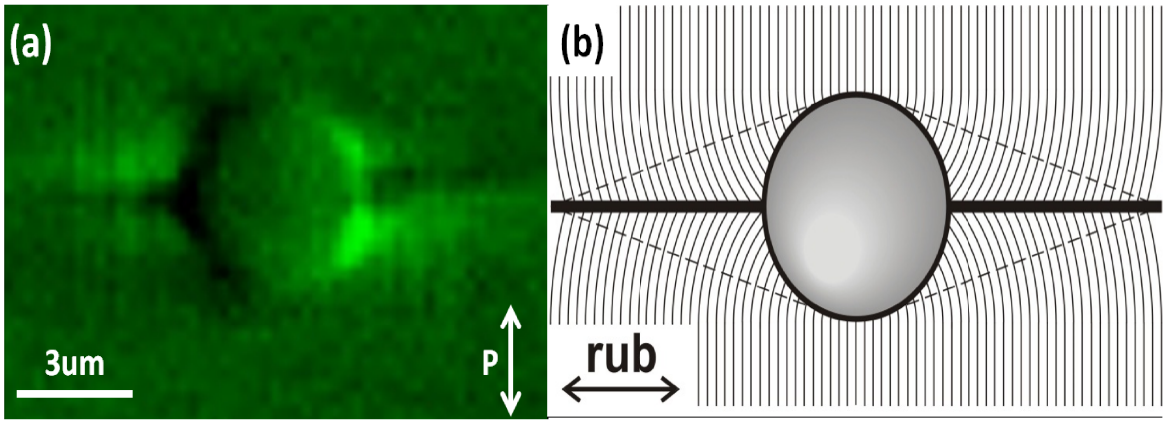

Figure 2.4.2 (a) shows an SRL microscopy image of induced defects and director distortions of a smectic LC around a colloidal resin sphere with planar surface anchoring. (b) is an illustration of the distortion of smectic layers in this type of system. Adapted from “Imaging of director fields in liquid crystals using stimulated Raman scattering microscopy,” by T. Lee, H. Mundoor, D. Gann, T. Callahan, and I. Smalyukh (2013).

3. Raman Signal Enhancement via Surface Plasmon Resonance

3.1 Idea and Motivation

Despite the advantages of CARS and SRL microscopy techniques they do have certain drawbacks. Both techniques require the use of high-speed, pulsed laser sources in order to obtain the necessary powers to significantly drive these processes. These types of pulsed, tabletop lasers can be quite expensive and sometimes also bulky. As such, we would like to be able to image LC systems using cheaper, continuous wave laser sources with much lower instantaneous powers.

Additionally, due to the still relatively weak signals from both CARS and SRL, identification of very small concentrations of materials is either not possible or would require extremely long acquisition periods to construct an image. Sufficiently low concentrations of some materials are even difficult to resolve in standard Raman spectroscopy. So it would also be helpful to have a tool capable of enhancing the entire Raman spectra, for sensitive identification of a wide range of constituents, instead of only probing specific Raman transitions as we do in SRL imaging. Better yet, if this new tool can be combined with SRL and CARS to provide additional Stokes and anti-Stokes Raman signal enhancement, then perhaps we can reduce some of the non-linear noise and broadband difficulties of CARS and also improve the signal to noise ratio of the SRL technique, potentially making it capable of faster or even live imaging.

One possibility for such a tool is the use of colloidal metal nano-particles, which can provide efficient light harvesting due to specially propagating modes along the metal surface known as surface plasmon polaritons. It turns out that these modes can couple to Raman transitions, and provide a significantly enhanced Raman signal due to the efficient uptake of

light energy. However, because of the surface confinement of these modes and the small dimensions of the colloidal metal particles, the enhancement effect is restricted to a small proximity about the particles. Yet, if we introduce some sort of manipulation, such as an optical trapping system, we can potentially maneuver these metal nano-particles to areas of interest within the sample thus allowing us to probe regions of interest.

3.2 Surface Plasmon Resonance

Metal-dielectric interfaces are capable of supporting specially propagating, electromagnetic modes, known as surface plasmon polaritons, which are carried along the conducting “skin” of the metal. These modes couple to photon frequencies in the visible and near infrared, whereby the electric field component of the incoming light excites a collective oscillation of the conduction electrons on the metal surface [29]. The oscillating electrons produce a charge separation and thus a polarity along the surface. This results in a propagating electric dipole, thus called a surface plasmon polariton (SPP) [29] [26] [28]. SPPs oscillate with the same frequency as the excitation light, but have a wavelength typically much shorter than that of the excitation photon [29]. The confinement of the electrons in the short-wavelength dipole then causes a strong electric field to emerge in the near field [23]. In accordance with Maxwell’s equations, this field penetrates much further into the dielectric than the metal. An illustration of a photon, incident on a metal from a dielectric medium, producing an SPP is given in figure 3.2.1.

In our experiments we use gold nanoparticles, which are orders of magnitudes more absorptive than even highly absorbing dyes. This allows for efficient conversion of the laser light energy into SPP modes. Due to their small dimension, they also undergo little internal

scattering and confine the light energy to small regions [23]. The small dimensions and highly curved surfaces of the nanoparticle also provide tight confinement of the SPP. This in turn allows for a very large electric field enhancement as compared to the electric field of the light in the absence of the metal surface [25] [26] [28]. Due to greater enhancement from sharply curved surfaces, we chose to use gold “nano-burst” (NB) particles which have a highly jagged and irregular surface [2]. A COMSOL simulation of the electric field enhancement due to two such NB particles is given in figure 3.2.2 (b). The simulation profiles were rendered from TEM images of actual gold NBs, shown in figure 3.2.2 (a) [2].

The enhanced electric field allows the SPP to cause greater distortion of bonds with varying polarizability [24][29]. This and the more efficient collection of light energy by the metal surface cause significantly greater transfer of energy into Raman active modes, effectively increasing the Raman cross section, σ_{Raman}, of nearby materials [23][24][26][28]. This type of enhancement is known as surfaced enhanced Raman scattering (SERS) [23][24] [26] [27][28][29]. When driven intentionally, the colloidal, gold nanoparticles effectively become nano-antenna that can couple optical energy to Raman active bonds of adhered and nearby molecules.

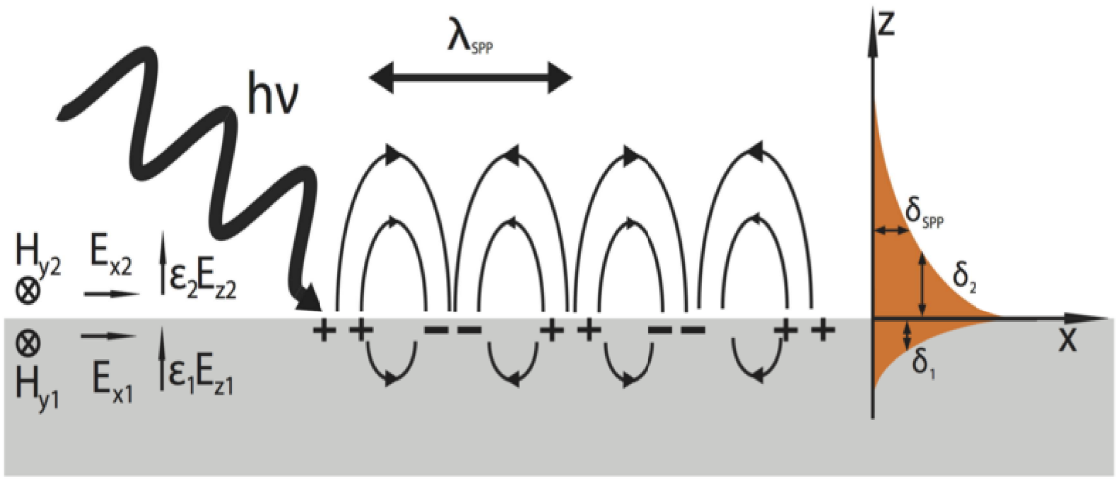

Figure 3.2.1. A illustration depicting an incident photon exciting a surface plasmon polariton (SPP) along a metal-dielectric interface. The + and – signs indicate charge separation of the electron plasma and the creation of an electric dipole/ plasmon polariton. The lines emanating from the charges show the electric field of the SPP. The relative size of the electric field lines indicate that the SPP field penetrates deeper into dielectric than the metal. Adapted from "Surface Plasmon," en.Wikipedia.org/wiki/Surface_plasmon, accessed on March 27, 2014.

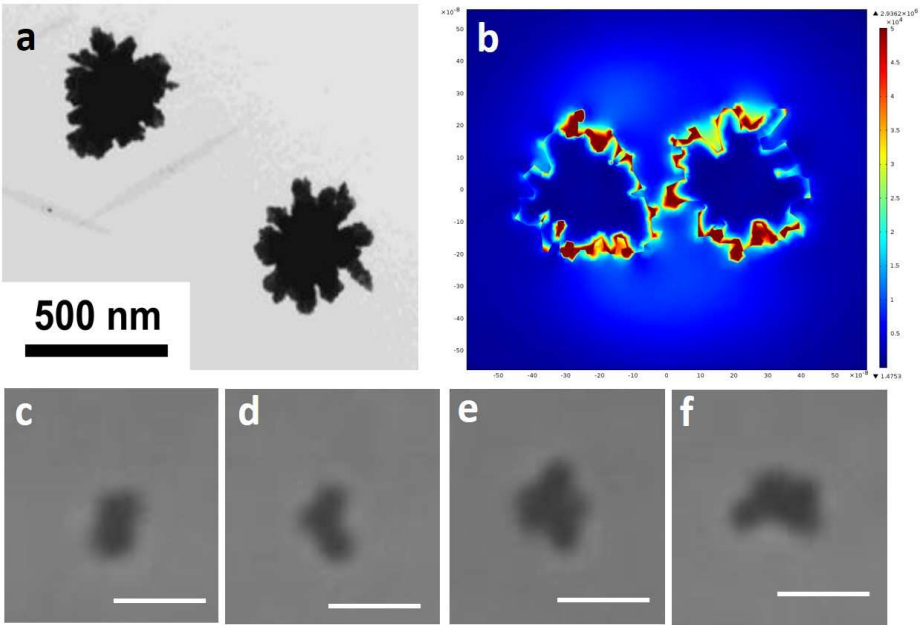

Figure 3.2.2 (a) shows a TEM image of two gold nano-burst (NB) particles. (b) shows a COMSOL simulation of the electric field enahncement around two profiles constructed from the NB particle images in (a). (c-f) are widefield, optical microscopy images of assemblies of 2, 3, 4, and 5 NB particles, respectively. These particles were assembled using our optical trapping system. Scale bars in (c-f) are one micron. Adapted from "Optically and elastically assembled plasmonic nano-antenae for spatially resolved characterization of chemical composition in soft matter systems using surface enhanced spontaneous and stimulated Raman scattering," by H. Mundoor, T. Lee, D. Gann, P. Ackerman, B. Senyuk, J. Lagemaat, and I. Smalyukh, (in preparation).

3.3 Optical Trapping and Manipulation

Early SERS experiments used metal coated substrates and direct probing with metallic tips. Since then, it has been demonstrated that efficient dispersions and reconfigurable self-alignment of colloid metal nanoparticles can be achieved in LC media [30] [31]. However, we can gain an additional level of control over our nano-antennae by introducing optical trapping and manipulation into our systems [32] [33] [35] [36]. Optical trapping can be understood as the interaction between focused light and opaque, colloidal particles which have a higher index of refraction than the surrounding medium.

For a particle sitting laterally from the beam focus, scattering by the particles will on average be uniform in every direction and as such will not produce a net force on the particle. However, if the particle is sitting in a gradient of optical intensity, i.e. displaced from the beam focus, there can be a net force generated on the particle due to uneven refraction. See figure 3.3.1 (a) for an illustration of this. Likewise, the force generated by forward scattering can pull a particle vertically, and the radiation pressure from absorption and reflection can produce pushing forces for particles sitting bellow and above the beam focus respectively [32]. The vertical forces are illustrated in figure 3.3.1 (b).

When these forces balance with other forces on the system, e.g. gravity or elastic free energy, they can produce a local energy minimum at the laser beam focus. We then have a three dimensional optical trap [32]. It has been shown that stable trapping only occurs for highly focused beams with strong gradients, and particles which aren’t strongly absorptive or reflective and which have a higher index of refraction than the surrounding medium [33].

The most common method for optical trapping employs a spatial light modulator (SLM) to control the phase front of an incoming laser beam [33] [34] [35] [36]. SLMs are specially

engineered liquid crystal devices that, with the assistance of clever software, allow for the production of user-designed holograms to be formed from the incident laser beam. As such, an optical trap can be produced and manipulated in three dimensions with the help of a spatial light modulator [33][34]. When combined with imaging optics, this allows for the trapping and manipulation of defects and colloids in the LC media in conjunction with our standard microscopy techniques [35][36]. This also affords for collocation of plasmonic metal nanoparticles, as discussed above, with regions of interest within the sample, effectively giving us a nano-scale probe for SERS. In the absence of a SLM and the necessary optics to properly construct the trap hologram [33], a static trap can be easily built around the same imaging optics and 3D plasmonic probe manipulation gained via precision stage movements [2]. We demonstrate our ability to optically manipulate colloidal nano-particles by creating an assembly of them, which is shown in figure 3.2.2 (c-f).

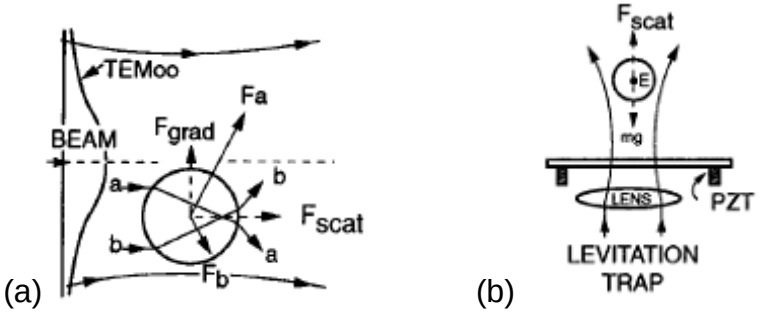

Figure 3.3.1. Force-body diagrams of the scattering and gradient forces on a small colloidal sphere in an optical gradient field, which produces the optical trapping force. Figure (a) demonstrates xy trapping of a particle displaced laterally from the beam focus do to gradient forces. Figure (b) demonstrates trap “lifting” (downward in this case) by forward scattering for a particle displaced vertically from the beam focus. Adapted from “Optical trapping and manipulation of neutral particles using lasers,” by Arthur Ashkin, *Proc. Natl. Acad. Sci. USA* **94**, 4853–4860 (1997)

3.4 SERS Nano-Probe Implementation

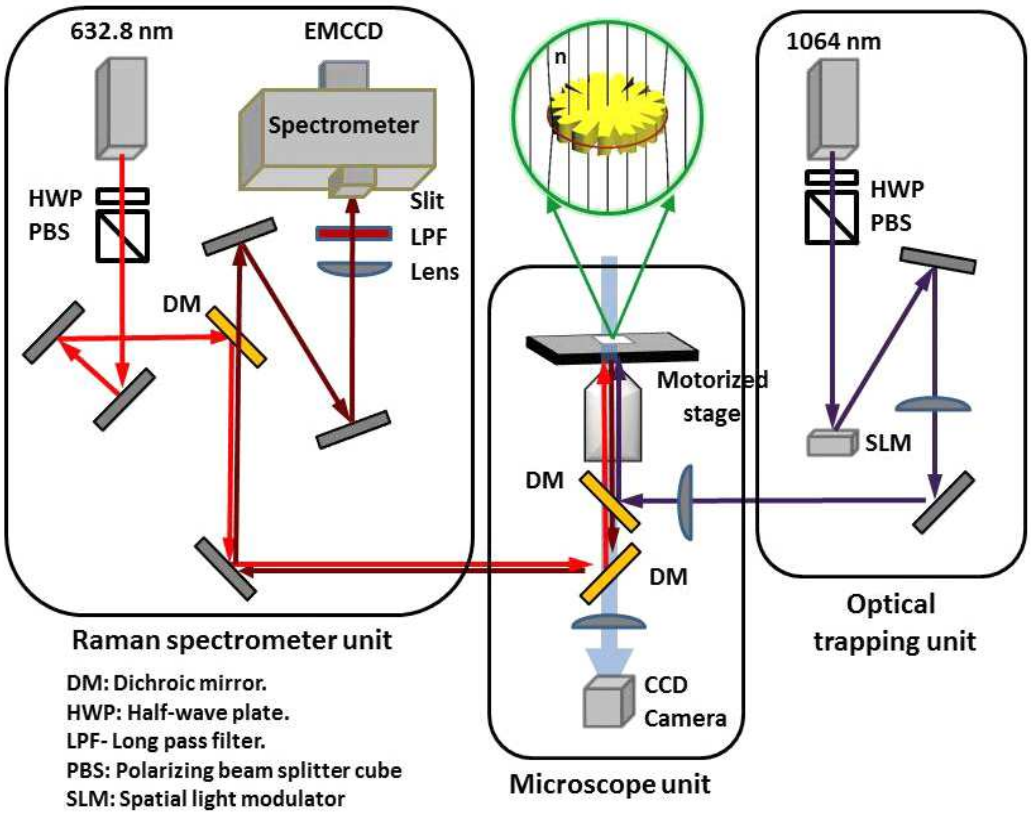

Figure 3.4.1. This is a simplified schematic of our SERS micro-probe setup. This system makes use of a static optical trap, produced by a 1064 nm laser and spatial light modulator and motorized stage to manipulate colloidal particles. The trap is built alongside a homemade Raman spectrometer, which consists of a 632.8 nm excitation beam, filtering optics, a commercial spectrometer unit with adjustable grating, and an electron-multiplying CCD camera. We also make use of low power white light and a cheap CCD camera to provide visual aid to the optical trapping and manipulation. Adapted from "Optically and elastically assembled plasmonic nano-antenae for spatially resolved characterization of chemical composition in soft matter systems using surface enhanced spontaneous and stimulated Raman scattering," by H. Mundoor, T. Lee, D. Gann, P. Ackerman, B. Senyuk, J. Lagemaat, and I. Smalyukh, (in preparation).

Figure 3.4.1 is a diagram giving a simplified layout of our SERS micro-probe setup. A 1064 nm laser source is polarized and sent through a spatial light modulator to produce a Laguerre-Gaussian beam profile which is then focused onto the sample for optical trapping. There is another low power, white-light illumination source, used in conjunction with a cheap CCD camera, to provide visual feedback to the user as he manipulates particles in the trap by

movement of the motorized stage. Another 632.8 nm laser, used as the Raman scattering source, is polarized and guided to the sample by the appropriate optics. The Stokes-Raman shifted light is then collected by the same objective, filtered out from the illumination, excitation, and trapping light, and sent into a commercial spectrometer. The spectrometer has an adjustable grating so that a wide range of Raman shifts can be accessed. Custom software was developed for fine control of the motorized stage to achieve trap manipulation. The software is also capable of running point-wise scans while triggering and acquiring data from the CCD, which could be used to construct images from a series of Raman spectra. However, we have not yet employed this capability in our studies. [2]

3.5 Characterization of the Optical Trap

In order to understand our SERS nano-probe system, we ran several tests to characterize of our optical trapping system. In the first of these tests we collect images of the Brownian motion of a NB particle within the optical trap and track its center of mass, for two orthogonal polarizations and a trapping power of 80 mW. We find that we can reasonably constrain the particle to a region roughly 400 nm by 100 nm for trap polarizations perpendicular to the far-field director, and to a region roughly 200 nm by 200 nm for trap polarizations parallel to the director. These displacement profiles are shown in figure 3.5.1 (a). In figure 3.5.1 (b) we plot the trap stiffness in $pN/\mu m$ as a function of laser power in mW, with the associated uncertainty in each measurement. The linear fit tells us we can reliably scale how confined a trapped particle will be over this range of optical powers. Figures 3.5.1 (c) and (d) demonstrate the rotational control capabilities of the holographic trap. Figure (c) shows the circular rotational displacement profile of a NB particle, trapped in a +3 Laguerre-Gaussian (LG) mode. Figure (d) shows how varied rotational speeds and directions can be achieved by altering the laser power and beam mode. The top plot is of a ± 3 LG mode , and the bottom for a ± 2 LG mode. The red, solid lines correspond to clockwise rotations and the blue, dashed lines correspond to counter-clockwise rotations. [2]

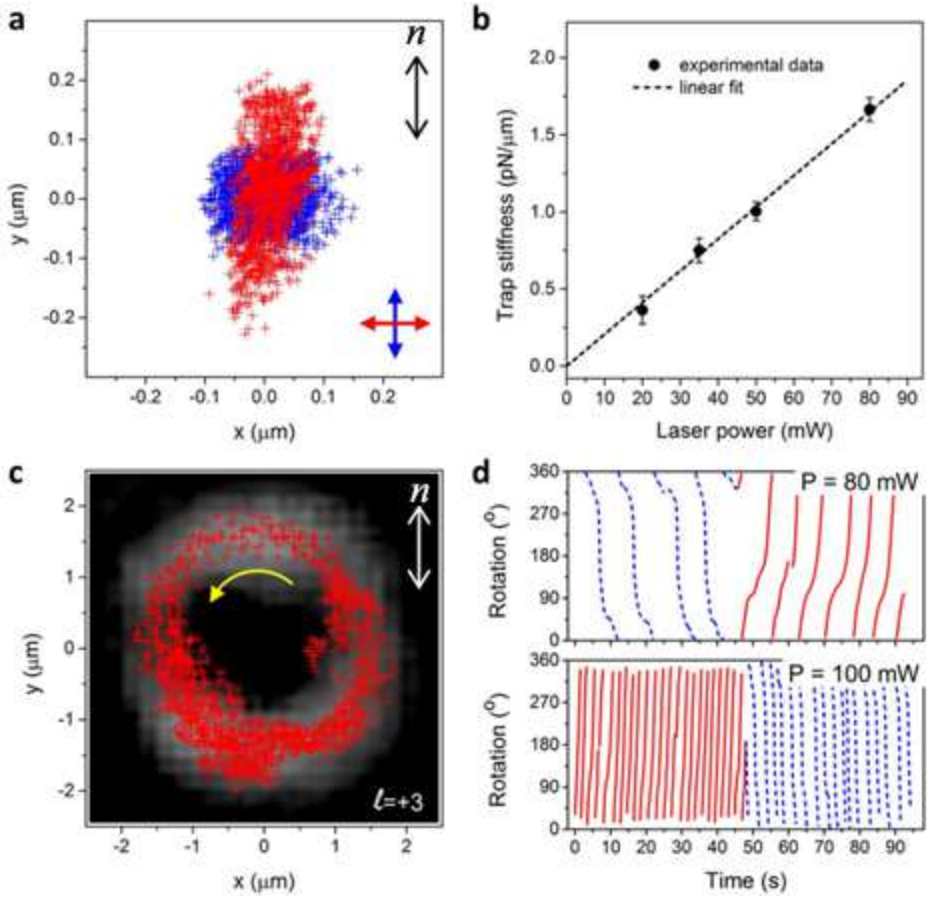

Figure 3.5.1. These figures give a characterization of our holographic optical trap. Figure (a) shows displacement profiles of a trapped NB particle for two orthogonal polarizations in an 80 mW trapping beam. Figure (b) shows a linear dependence of the trap stiffness with laser power. Figure (c) shows the counter-clockwise, circular rotation profile of a NB particle in a +3 Laguerre-Gaussian (LG) mode. Figure (d) shows varying rotational speeds for a ± 3 LG mode at 80 mW (top) and for a ± 2 LG mode at 100 mW (bottom). The red, solid lines in (d) represent clockwise rotations and the blue, dashed lines represent counter-clockwise rotations. Adapted from "Optically and elastically assembled plasmonic nano-antenae for spatially resolved characterization of chemical composition in soft matter systems using surface enhanced spontaneous and stimulated Raman scattering," by H. Mundoor, T. Lee, D. Gann, P. Ackerman, B. Senyuk, J. Lagemaat, and I. Smalyukh, (in preparation).

3.6 Demonstration of SERS Enhancement in Liquid Crystal Media

We prepared a sample of planar-aligned nematic LC, 5CB, with gold nano-particles dispersed in the bulk of the material. The sample was first placed into our Raman spectrometer to obtain the spectra shown in figure 3.6.1. Spectrum 3.6.1 (a) is of the 5CB bulk, i.e. the pure 5CB Raman spectrum. Spectrum 3.6.1 (b) was taken with a cluster of NB particles in the excitation beam. Spectrum 3.6.1 (c) was taken of NB particles spin-coated to a glass substrate.

The dashed lines indicate the origins of various peaks in the combined 5CB-NB spectrum. From this we can see that the additional peaks beneath the enhanced 5CB spectrum are coming from the thin capping ligands on the gold particles. The relative peak heights between figures 3.6.1 (a) and 3.6.1 (b) for the 5CB Raman lines shows there is a roughly 40 times stronger signal in the presence of NB particles.

We then imaged a cluster of NB particles in the bulk of a homeotropically aligned 5CB sample in our combined SRL/ CARS microscope. The images we obtained are shown in figure 3.6.2. Figure 3.6.2 (a) is an SRL image of the nano-burst particle from the side, and the inset in (a) gives an image of the particle cross-section. Figure 3.6.3 (a) is a complimentary CARS image of the same cluster, and 3.6.3 (b) is a superposition of (a) and (b). From this we can see that the SERS signal sufficiently enhances our higher-order imaging signals as well. [2]

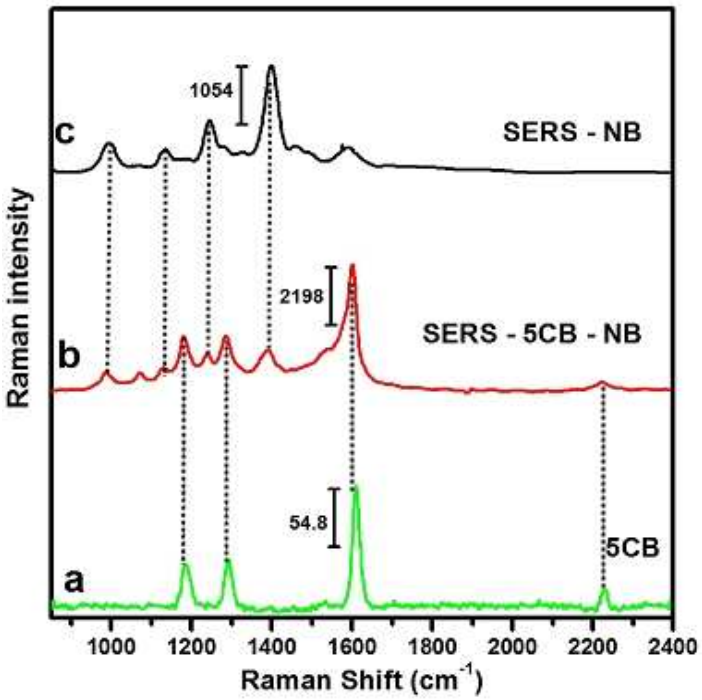

Figure 3.6.1 These are Raman spectra taken of (a) bulk, nematic 5CB LC, (b) a small cluster of NB particles in the 5CB LC bulk, and (c) of NB particles spin-coated to a glass substrate. The relative peak heights from (a) to (b) show significant signal enhancement of the 5CB spectrum. The peaks in (c) corresponding to the capping ligands indicate the origin of the additional peaks in the 5CB-NB spectrum. Adapted from "Optically and elastically assembled plasmonic nano-antenae for spatially resolved characterization of chemical composition in soft matter systems using surface enhanced spontaneous and stimulated Raman scattering," by H. Mundoor, T. Lee, D. Gann, P. Ackerman, B. Senyuk, J. Lagemaat, and I. Smalyukh, (in preparation).

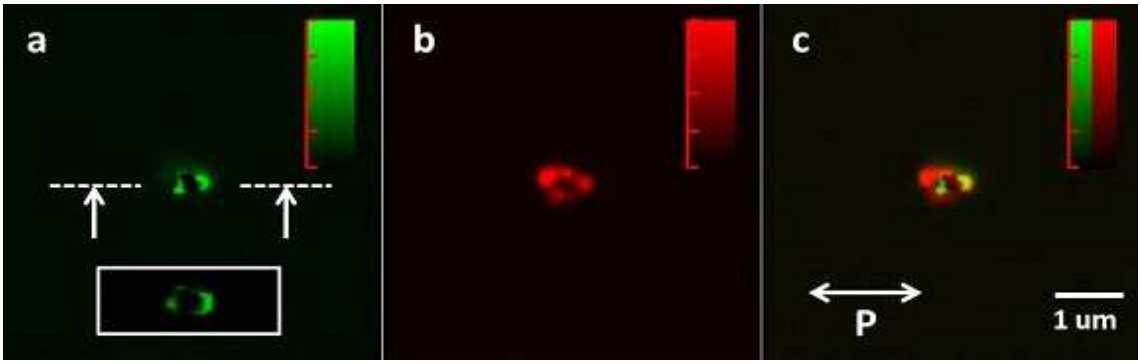

Figure 3.6.2. Microscopy images of a NB cluster in homeotropically aligned 5CB LC sample. Image (a) was obtained with the SRL technique presented in section 2. Image (b) was obtained with the CARS technique described in section 1.8. Image (c) shows the superposition of the two complimentary images. Adapted from "Optically and elastically assembled plasmonic nano-antenae for spatially resolved characterization of chemical composition in soft matter systems using surface enhanced spontaneous and stimulated Raman scattering," by H. Mundoor, T. Lee, D. Gann, P. Ackerman, B. Senyuk, J. Lagemaat, and I. Smalyukh, (in preparation).

3.7 Maneuverable Nano-Probes for Identification of Low Molecular Concentrations

Our next goal was to use these NB particles as a maneuverable nano-probe in our combined trapping/ Raman spectrometer system. In figure 3.2.2 (c-f) we already show that we are able to trap and assemble NB particles, but now we present an application of this capability in using our NB particles to probe very small concentrations of certain molecules. We do this first for identification of the capping ligands on short gold nanorods (sub-micrometer sized, colloidal gold rods). Second we show the capability of using NB particles to determine the relative concentrations of small polymer chains inside and outside LC defects.

Two samples were prepared, both contained dispersed NB particles and short gold nanorods (SR, standing for short rods) but in one the nanorods were capped with modular polyethylene glycol (mPEG) and in the other the rods were capped with polystyrene (PS). Figure 3.7.1 (a) is of the Raman spectrum of a cluster of NB particles in the 5CB bulk. Figures (b) and (c) show the Raman spectra of single SR particles surrounded by assemblies of NBs. In figures (b) and (c), the SR were capped with mPEG and PS, respectively. The dashed lines represent the characteristic Raman spectra of the two different capping ligands. The dashed peaks clearly show matching peaks with the obtained spectra that don’t belong to 5CB or the NSOL capping on the NB particles. This indicates that we were successfully able to identify very low concentrations of different capping materials, which are typically only a single molecular layer thick.

We again prepared a sample of 5CB LC with dispersed NB particles, but this time we included a reactive mesogen (RM) that can be optically stimulated to link into a polymer chain. After checking for reasonable dispersion of NBs and that a decent number of NBs were located in defect structures, we partially polymerized the sample to a polymer-5CB ratio of

3:7. We then obtained SERS spectra from NB particles located in the LC bulk and NB particles located within a defect core. These spectra are shown in figures 3.7.2 (b) and (c) respectively. When these are compared to the Raman spectrum of just the reactive mesogen (figure 3.7.2 (a)) we see there are two distinct peaks of the mesogen, indicated by the dashed lines, which are not obscured by the 5CB spectrum, indicated by the stars. We also see that the RM peaks are far stronger for the SERS spectra obtained from the NB filled defect cores than from bulk NB clusters. This indicates an affinity for the partially polymerized chains to locate in the isotropic regions at the centers of defects. This also demonstrates the SERS nano-probe's capability to identify small variations in chemical concentrations, such as the reactive mesogen in a partially polymerized material. [2]

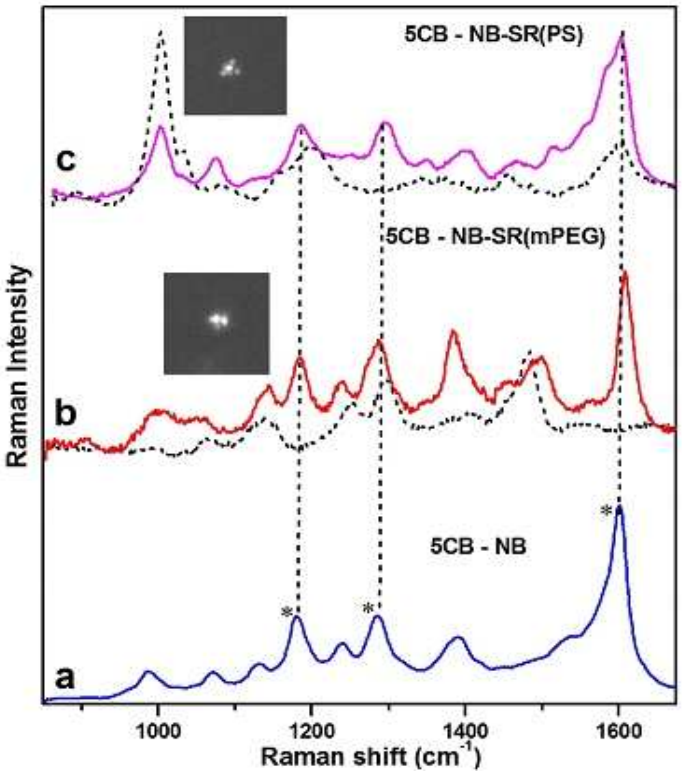

Figure 3.7.1 Shown here are Raman spectra of (a) NB particles in the 5CB LC bulk, (b) NB particles assembled around mPEG capped short nanorods (SRs) in 5CB LC, and (c)) NB particles assembled around PS capped SRs in 5CB LC. Dashed lines and stars lie on the characteristic 5CB Raman spectral lines. The dashed curves represent the 5CB-NB-SR spectra after subtracting the 5CB-NB spectrum. The insets in (b) and (c) show dark-field microscopy images of the NB-

SR assemblies, which were constructed via optical trapping. Adapted from "Optically and elastically assembled plasmonic nano-antenae for spatially resolved characterization of chemical composition in soft matter systems using surface enhanced spontaneous and stimulated Raman scattering," by H. Mundoor, T. Lee, D. Gann, P. Ackerman, B. Senyuk, J. Lagemaat, and I. Smalyukh, (in preparation).

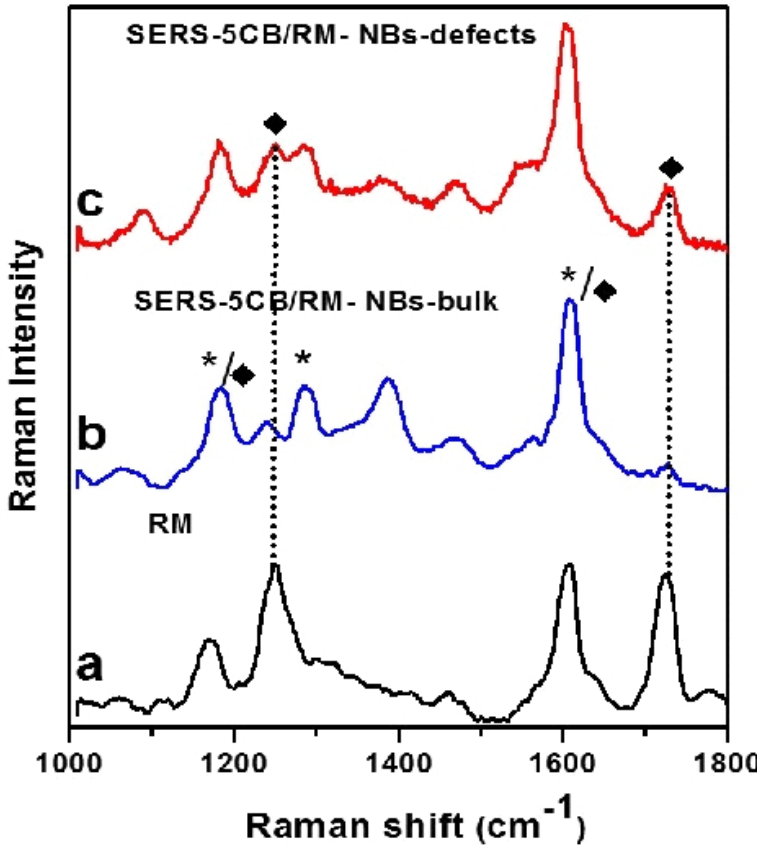

Figure 3.7.2. Shown here are the Raman spectra of (a) the polymer-forming reactive mesogen (RM), and a sample prepared with 5CB LC, dispersed NB particles, and RM that is partially polymerized to a ratio of 3:7. The spectra (b) and (c) show the SERS signal obtained from NB assemblies in the LC bulk and in the core of a defect, respectively. The squares and stars label characteristic peaks of the RM and 5CB LC, respectively. The dashed lines show two peaks of the RM spectrum which are stronger in the defect spectrum than in the bulk LC spectrum. This indicates that the partially polymerized, linked by the mesogens, prefers the isotropic regions of the sample. Adapted from "Optically and elastically assembled plasmonic nano-antenae for spatially resolved characterization of chemical composition in soft matter systems using surface enhanced spontaneous and stimulated Raman scattering," by H. Mundoor, T. Lee, D. Gann, P. Ackerman, B. Senyuk, J. Lagemaat, and I. Smalyukh, (in preparation).

4. Conclusion

Non-invasive, three-dimensional imaging of LC-colloid systems is possible through the use of multiple-photon fluorescence and coherent anti-Stoke Raman scattering techniques. However, these techniques suffer from broad spectral peaks and non-resonant background signal. To improve imaging capabilities for highly chemically sensitive and low noise imaging, we employ a stimulated Raman scattering technique. In this technique we use a single laser to pump vibrational modes of the molecule with one beam and stimulate Stokes-Raman transitions with a tunable, broadband beam. The tunable beam allows us to target specific vibrational modes of interest. The stimulated emission is then modulated and the corresponding modulated loss in Rayleigh-scattered pump light is detected by a lock-in amplifier, a technique we call stimulated Raman loss (SRL). The amplifier is triggered in conjunction with a slow, stage-scanning algorithm in order to later construct images. We first characterize our SRL microscope. We then demonstrate its ability to image director structure around LC defects as well as colloidal distortions of director fields, and how it obtains complimentary, lower-noise signals than CARS while also being able to be implemented alongside it.

We also demonstrate the use of dispersed, colloidal gold nano-burst (NB) particles in combination with holographic optical trapping as a maneuverable nano-probe for sensitive chemical identification. We present a characterization of the optical trapping system and its capability of assembling NB in a LC host. We then show the significant enhancement provided by the surface enhanced Raman scattering (SERS) of the metal surface plasma, resulting in a ~40 fold increase in Raman intensity of the 5CB Raman spectrum, as well as significantly improved SRL and CARS signals. We then demonstrate the nano-probe system’s capabilities by detecting two distinct, molecule-thin capping layers on short gold nanorods. We also show that the nano-probe is capable of sensing low concentrations of partially polymerized materials and that these concentrations differ slightly between

the bulk LC and the isotropic LC defect cores.

These two new tools provide greater capability for imaging director structure and enhancing Raman signals, even for very low concentrations of materials. Scientists and engineers who study soft matter can use these techniques to better understand what is happening in their systems. In turn they will be able to produce better science and technology which will in turn benefit society as a whole, as new LC based technologies enter our lives.

Acknowledgments

I would like to give a special thanks to my thesis adviser Dr. Ivan Smalyukh for being immensely helpful over the last two year, as well as Dr. Taewoo Lee, Dr. Haridas Mundoor, Dr. Bohdan Senyuk, Paul Ackerman, and Timothy Callahan for all contributing to the work presented here. I would also like to thank Dr. Jao van de Lagemaat for the COMSOL simulations he provided for our paper in preparation, as well as all other members of the Smalyukh group for always being around to help, answer questions and have discussions. Portions of this work were sponsored by the UROP program, the Discovery Learning Apprenticeship program, and an NSF grant.

Bibliography:

1: T. Lee, H. Mundoor, D. Gann, T. Callahan, and I. Smalyukh, "Imaging of director fields in liquid crystals using stimulated Raman scattering microscopy," *Opt. Express* 21, 12129-12134 (2013).

2: H. Mundoor, T. Lee, D. G. Gann, P. J. Ackerman, B. Senyuk, J. van de Lagemaat, & I. I. Smalyukh. "Optically and elastically assembled plasmonic nano-antenae for spatially resolved characterization of chemical composition in soft matter systems using surface enhanced spontaneous and stimulated Raman scattering." *In preparation* (2014).

3: David Sidebottom, "Fundamentals of Condensed Matter and Crystalline Physics," Cambridge Univ. Press, (2012)

4: "Liquid Crystals". *Nobelprize.org.* Nobel Media AB 2013. Accessed on Web, 18 Mar 2014. <http://www.nobelprize.org/educational/physics/liquid_crystals/history/>

5: P. Oswald and P. Pieranski, "Nematic and Cholesteric Liquid Crystals," Taylor & Francis, (2005)

6: P. G. De Gennes & J. Prost, "The Physics of Liquid Crystals," Oxford Univ. Press, (1995)

7: O. D. Lavrentovich, "DEFECTS IN LIQUID CRYSTALS: SURFACE AND INTERFACIAL ANCHORING EFFECTS," *Patterns of Symmetry Breaking*, 161-195 (2003).

8: N. Lebovka et. al., "Low temperature phase transformations in 4-cyano-4'-pentylbiphenyl (5CB) filled by multiwalled carbon nanotubes," *Physica E* **52**, 65-69 (2013).

9: I. Smalyukh et. al., "Focused laser beams and liquid crystals: fast three-dimensional imaging of structures and topological defects," Proc. of SPIE **Vol. 5947**, 594707-1 (2005).

10: B. A. Averill & P. Eldredge, Ch. 11.8 "Liquid Crystals," *Principles of General Chemistry*, Licensed under Creative Commons nc-sa-3.0, (2012), Accessed 18 March 2014.

11: C. Xiang & A Barron, "The Analysis of Liquid Crystal Phases using Polarized Optical Microscopy," Creative Commons Attribution License, **module: m38343**, (2011)

12: H. Ehrentraut, "Overview of the mesoscopic theory of liquid crystals," *Institut für Theoretische Physik*, (1997), <https://wwwitp.physik.tu-berlin.de/muschik/liquid_crystals/lc_intro.html>, Accessed on March 19, 2014.

13: Q. Liu et. Al. "Self-Alignment of Plasmonic Gold Nanorods in Reconfigurable Anisotropic Fluids for Tunable Bulk Metamaterial Applications" *NanoLetters **10*** (4), 1347–1353 (2010)

14: I. Smalyukh, S. Shiyanovskii, and O. Lavrentovich, "Three-dimensional imaging of orientational order by fluorescence confocal polarizing microscopy," *Chem. Phys. Lett.* **336**(1–2), 88–96 (2001).

15: P. Campagnola, L. M. Loew, "Second-harmonic imaging microscopy for visualizing biomolecular arrays in cells, tissues and organisms," *Nature Biotechnology* **21 (11)**, 1356-1360 (2003)

16: C.V. Raman, K.S. Krishnan, "A New Type of Secondary Radiation," *Nature* 121, 501-502 (1928).

17: C. Freudiger et. Al. “Label-Free Biomedical Imaging with High Sensitivity by Stimulated Raman Scattering Microscopy” *Science* 19, 1857-1861 (2008).

18: A. Kachynski et. Al. “Coherent anti-Stokes Raman scattering polarized microscopy of three-dimensional director structures in liquid crystals” *App. Phys. Lett.* 91, 151905 (2007).

19: S. Thomas, “Infrared and Raman Spectroscopy,” Teaching Mineralogy, sponsored by University of Nevada Las Vegas, (2013) accessed from http://serc.carleton.edu/NAGTWorkshops/mineralogy/mineral_physics/raman_ir.html#IR on March 25, 2014

20: Cheng et. al., “Laser-Scanning Coherent Anti-Stokes Raman Scattering Microscopy and Applications to Cell Biology,” Biophysical Journal 83, 502-509 (2002)

21: Duncan et. al., “Scanning Coherent anti-Stokes Raman Microscope,” Optics Letters 7 (8), 350-352 (1982)

22: G. Fowles, “Introduction to Modern Optics” 2nd ed., Dover Publications, (1975)

23: S. Eustis and M. A. El-Sayed, “Why gold nanoparticles are more precious than pretty gold: Noble metal surface plasmon resonance and its enhancement of the radiative and nonradiative properties of nanocrystals of different shapes” Chem. Soc. Rev. 35, 209–217 (2006).

24: S. McCall and P. Platzman, “Surface enhanced Raman scattering,” *Physics Letters* **77A (5)**, 381-383 (1980)

25: E. Hao et. al., “Synthesis and Optical Properties of Anisotropic Metal Nanoparticles,” *J. of Fluorescence* **14 (4)**, 331-341 (2004)

26: E. Ru et. al., “Surface Enhanced Raman Scattering Enhancement Factors: A Comprehensive Study,” *J. Phys. Chem*. **111**, 13794-13803 (2007)

27: S. Nie and S. R. Emory, “Probing Single Molecules and Single Nanoparticles by Surface-Enhanced Raman Scattering,” *Science* **275 (5303)**, 1102-1106 (1997)

28: Q. Sun et. al. “Plasmon-Enhanced Energy Transfer for Improved Upconversion of Infrared Radiation in Doped-Lanthanide Nanocrystals,” Nano Lett. 14, 101-106, a publication of the American Chemical Society (2013)

29: S. Zeng et. al., “Nanomaterials enhanced surface plasmon resonance for biological and chemical sensing applications,” Chem. Soc. Rev., DOI: 10.1039/c3cs60479a, The Royal Society of Chemistry (2014)

30: Qingkun Liu et. al., “Self-Alignment of Plasmonic Gold Nanorods in Reconfigurable Anisotropic Fluids for Tunable Bulk Metamaterial Applications,” *Nano Lett.* 10, 1347-1353 (2010).

31: R. Pratibha et. al., “Colloidal gold nanosphere dispersions in smectic liquid crystals and thin nanoparticle-decorated smectic films,” *J. of Applied Physics* 107, 063511 (2010).

32: Arthur Ashkin, “Optical trapping and manipulation of neutral particles using lasers,” *Proc. Natl. Acad. Sci. USA* **94**, 4853–4860 (1997)

33: Suman Anand et. al., “Non-contact optical control of multiple particles and defects using holographic optical trapping with phase-only liquid crystal spatial light modulator,” Proc. of SPIE **Vol. 7232**, *Emerging Liquid Crystal Technologies* IV (2009).

34: Ivan Smalyukh et. al., “Optical trapping of director structures and defects in liquid crystals using laser tweezers” *Optics Express* 15 (7), 4359-4371 (2007).

35: Rahul Trivedi et. al., “Three dimensional optical manipulation and structural imaging of soft materials by use of laser tweezers and multimodal nonlinear microscopy,” *Optics Express* 18 (26), 27658 (2010).

36: Donald Conkey et. al., “Three-dimensional parallel particle manipulation and tracking by integrating holographic optical tweezers and engineered point spread functions,” *Optics Express* **19 (5)**, 3835 (2011).